

Response to T. Aoki (Reviewer #1)

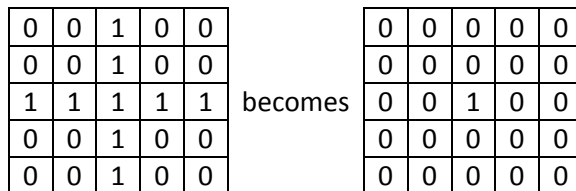
We thank very much T. Aoki for the positive evaluation of our work and for his thorough revision, with punctual comments and corrections. Here below are our answers to each of his comments (Aoki's comments are in bold).

Main comments:

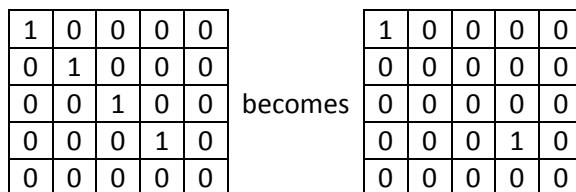
(1) The detailed procedure to obtain a snow particle size metric is a bit hard to understand. How are the skeleton's endpoints determined? The skeleton branch shown in Fig. 6b looks not a straight line but a curve. The white curves in the particles in Fig. 6b do not correspond to the inner structure of the snow particles in Fig. 6a. I do not understand which parts do the red skeleton branches in Fig. 6b correspond to in Fig. 6a as well.

We tried to improve the description of the procedure we followed to calculate the SSK metric, modifying the text as (p.14, line 29): *“For each particle, we determined the skeleton by successively removing pixels on the boundary, without letting the particle to break apart (using the automatic routine “bwmorph” of the Matlab Image Processing Toolbox). Endpoints and branch points were then identified as the extremities and the junction nodes of the skeleton branches, respectively (Fig 6b). We calculated the lengths of skeleton branches as the Euclidean distances between the skeleton's endpoints and their nearest branch points, and we selected the shortest skeleton branch (SSK) as the particle metric (Fig. 6b).”* The skeleton of each particle is determined on the basis of the particle mask, i.e. its 2D particle projection, therefore it does not correspond to the grain structure visible in the photo. The skeleton only describes the geometrical structure of the particle projection. Here below are examples of how the endpoints and branch points are calculated:

Find branch points of skeleton:



Find end points of skeleton:



We modified Figure 6, replacing Fig. 6b with the zoom of two detected particles, and rewrote the figure caption as: *“Example of a segmented image from 29 December 2009: the segmented outlines are overlaid with the original image (a), and two detected particles are magnified (b) to*

illustrate the skeleton (inner white lines), the skeleton endpoints (white dots at the particle border), and branch points (white dots at the junction nodes of the skeletons). The shortest of the skeleton branches, defined here as the Euclidean distances between endpoints and nearest branch point, are marked in red and correspond to the SSK metric."

- (2) It should be described that the effect of snow impurities on albedo can be ignored in section 3.3 as soot concentration in Antarctica is very low (e.g., Warren and Clarke, 1990).**

In Sect. 3.3 we added the sentence (p.18, line 18): "*When modelling surface albedo, snow is considered pure, as soot concentration in Antarctica is so low as to be optically insignificant (Warren and Clarke, 1990).*"

- (3) The discussion on refractive index of ice is too short to exclude it as the possible cause of discrepancy between modeled albedo and measurement or between r_{eff} and r_{oeff} .**

In the revised paper, we replaced the short discussion at p. 3438, lines 5-7, with the following text (p.28, line 26): "*On the basis of our results, we cannot exclude the possibility that uncertainties in ice refractive index may contribute to the wavelength dependence of r_{oeff} . If this were the main reason for the wavelength dependence, we would expect that the relative differences in r_{oeff} between different wavelengths are similar from case to case. Indeed, we note from Fig. 11 that the best estimate of r_{oeff} at $\lambda=2.20 \mu\text{m}$ is consistently slightly larger than that at $\lambda=1.70 \mu\text{m}$ (in relative terms, by 13-20% depending on case). However, the difference in r_{oeff} between the weakly absorbing wavelengths ($\lambda=1.05 \mu\text{m}$ and $\lambda=1.28 \mu\text{m}$) and $\lambda=1.70 \mu\text{m}$ depends strongly on the case: the relative difference between $\lambda=1.05 \mu\text{m}$ and $\lambda=1.70 \mu\text{m}$ varies from 45 to 391%, and that between $\lambda=1.28 \mu\text{m}$ and $\lambda=1.70 \mu\text{m}$ from 53% to 158%. This strong case dependency suggests that uncertainties in refractive index are probably not the primary contributing factor to the wavelength dependence of r_{oeff} .*"

Specific comments:

p. 3409, L18: Add reference Aoki et al. (2011), which demonstrated a long-term broadband albedo successfully simulated with a physically based snow albedo model using the measured shortest snow grain dimension.

Done

p. 3415, L11: Fig. 3b appears before Fig. 3a.

Indeed the reference to Fig 3a was missing. We added the reference (p.8, line 30): "*...extended from the surface to the depth of 5 cm (the surface appearance on 29 December is shown in Fig. 3a).*"

p. 3415, L16: Delete "s" at the end of this line.

Done

p. 3416, L26-27: "an almost-Lambertian white panel" Is it Spectral reflectance target? Please indicate in more detailed.

We replace "white panel" with "Spectralon target".

p. 3417, L1-3: “Snow and reference radiances were acquired using the ASD bare fore optic (with a nominal field of view of 25°) pointing toward nadir,” and Fig. 3: Did authors actually confirm the tripod’s feet were not included in FOV of the bare fiber? The instrument could have sensitivity at even outer angles of the nominal FOV of 25°.

Indeed, we realized that the ASD spectro-radiometer is sensitive to a FOV that is larger than the nominal one, especially in the VNIR region. This is the reason why we could not use the VNIR measurements, as in our setup the distance between the Spectralon target and the fore optic was just sufficient to cover the nominal FOV of the ASD, but insufficient to completely cover the real FOV of the ASD. We believe that the legs of the tripod did not interfere at all with the snow reflectance measurements, as the fore optic head pointed in the middle of the distance between two legs, which, at the surface level, was about 80cm. As the fore optic head was at about 1-m height above the surface, the nominal FOV had a radius of about 22 cm. Although the real FOV was larger, we think that it was not as large as the ~50° that would be needed to include the legs.

p. 3417, L26: “The horizontal leveling of the reference panel was checked with a bubble balancer.” The same explanation is made on L17.

We removed this sentence.

p. 3417, L27-29: “The uncertainty of snow reflectance related to the horizontal levelling of the reference panel (σ_{ref}) was +3% (+4 %) in the SWIR1 (SWIR2) wavelength region, estimated as the normalized standard deviation of 30 consecutive spectra of reference reflectance.” Why can “the uncertainty related to the horizontal levelling of the reference panel” be estimated from “the normalized standard deviation of 30 consecutive spectra”? It may be related to uncertainty of the spectrometer itself.

The repeatability error of the reference reflectance (reflectance from the Spectralon), calculated as the normalized standard deviation of 30 consecutive spectra, was larger (about double) than the repeatability error of the snow reflectance (σ_{rpt}), calculated as the normalized standard deviation of the snow reflectance among the 30 spectra. If only instrumental uncertainties were involved, the repeatability should have been similar for the snow and the Spectralon reflectances, but in fact we expected the Spectralon reflectances to be more inaccurate, as the Spectralon was held manually (and, thus, not perfectly steadily) during the 30 consecutive measurements, the horizontal levelling being maintained by the operator by checking the bubble balancer. To explain better this error, we rewrote the paragraph and moved it after the paragraph describing σ_{rpt} (p.12, line 9): *“The repeatability of the reference reflectance (σ_{ref}), calculated as the normalized standard deviation of 30 consecutive spectra of reference reflectance, was $\pm 3\%$ ($\pm 4\%$) in the SWIR1 (SWIR2) wavelength region. This uncertainty is larger than σ_{rpt} , and is presumably attributable to the inaccuracy of the manual horizontal levelling of the Spectralon plate.”*

p. 3420, L23: “712 x 1078 pixels” is better to be “1078 x 712 pixels” because of the consistency to the original resolution “4272 x 2848 pixels” on L18.

Corrected

p. 3421, L17: “The false snow particles” Please indicate them in Fig. 6a.

False snow particles were present only occasionally, not in all segmented photos. For instance there were no false particles in the photo selected for Fig 6a. We added the term “occasionally” at p.3421, line 19 to clarify this point.

p. 3424, L2: “Appendix B” appears before Appendix A.

Sorry for that, we now switched Appendices A and B to follow the order of appearance.

p. 3427, L9-10: “it is unlikely that droxtals (let alone spheres) would represent the phase function of snow particles accurately” Please indicate the reference or explain in more detail.

In some sense, this is almost self-evident: since snow consists of mainly irregular particles with varying morphology, it would be rather surprising if the phase function could be represented accurately by using droxtals, spheres or any other idealized shape. But this statement can also be justified by the fact that the phase function for droxtals, and especially spheres, differs substantially from the phase function

for blowing snow considered in Räisänen et al. (2015) (cited in the manuscript). In the revised manuscript, this is written as (p.19, line 14): *“On one hand, based on comparisons with a measured phase function for blowing snow (Räisänen et al. 2015), it is unlikely that droxtals (let alone spheres) would represent the phase function of snow particles accurately.”*

p. 3427, L11-13: “for the intermediate solar zenith angles considered here ($\theta_0 \approx 50^\circ - 60^\circ$), the Henyey–Greenstein phase function and the full phase function give quite similar results for snow albedo, with differences generally well below 0.01.” Please indicate the reference.

We checked this ourselves by comparing albedo calculations for optically thick snow made using the full sphere and droxtal phase functions and the corresponding Henyey-Greenstein phase functions (as a function of wavelength and snow grain size, assuming a monodisperse size distribution in these calculations). In light of earlier research, this is actually expected. In particular, Boucher (1998) showed that in the context of aerosol radiative forcing, the Henyey-Greenstein phase function works best at the intermediate solar zenith

angles most relevant for this study ($\theta_0 \approx 50^\circ - 60^\circ$). In the revised manuscript, this is written as (p.19, line 16): *“On the other hand, in line with the findings of Boucher (1998) for aerosol radiative forcing (Fig. 6 in that paper), the differences in snow albedo computed with the full phase function and the Henyey-Greenstein phase function are small at the intermediate solar zenith angles ($\theta_0 \approx 50^\circ - 60^\circ$) considered here (in fact, generally below 0.01 for both droxtals and spheres).”*

REFERENCE:

Boucher, O.: On aerosol direct shortwave forcing and the Henyey–Greenstein phase function. J. Atmos. Sci., 55, 128–134, 1998.

p. 3434, L22-24: “Thus, we can conclude that our method is suitable to measure the particle dimension that best corresponds to its scattering properties.” This result should be concluded after the discussion of spectral difference between r_{eff} and r_{oeff} .

Indeed, our statement was too strong and not yet justified by the discussion. In that section we only discuss the method applied to estimate the snow particle metric. Without drawing conclusions and only by looking at the results, we can replace the sentence with (p.25, line 29): *“This supports the hypothesis that our method is suitable to measure the particle dimension that best corresponds to its scattering properties.”*

p. 3437, L16: “Aoki, 2000” -> “Aoki et al., 2000”

Corrected

p. 3445, L10-11: “an effective solar zenith angle of 55° for the I_n measured in overcast conditions” Please indicate the reference for the values of 55° or mention the reason.

We acknowledge that this is a somewhat ad-hoc choice. It is based on the notion of the diffusivity factor, which is used to characterize the angular distribution of diffuse (scattered) radiation in two-stream radiation schemes, and which typically takes a value of $D=1.5...2$ (Edwards and Slingo, 1996). This would correspond to an effective zenith angle of $\theta_{0,eff} = \cos^{-1}(1/D) = 48.2^\circ - 60^\circ$. Finding out the optimal value in the present context would require very detailed radiative transfer computations including both the snow and the atmosphere with clouds, which we have not attempted. It may be noted, however, that changing $\vartheta_{0,eff}$ in Eq. (B5) in this range would change the resulting snow albedo at most by 3-4% compared to the results for $\theta_0=55$ deg. Discussion of this is added to the end of Appendix B in the revised manuscript (p.37, line 3): *“... using and effective zenith angle ($\vartheta_{0,eff}$) of 55° for the I_n measured in overcast conditions. This is somewhat an ad-hoc choice, based on the notion that in two-stream approximations in which the angular distribution of diffuse radiation is not represented explicitly, it is typically approximated with a diffusivity factor of $D=1.5-2$ (Edwards and Slingo, 1996), corresponding to an effective zenith angle of $\theta_{0,eff} = \cos^{-1}(1/D) = 48.2^\circ - 60^\circ$. Varying $\vartheta_{0,eff}$ in this range in Eq. (B5) would change the resulting snow albedo at most by 3-4% compared to the results for $\vartheta_{0,eff} = 55^\circ$.”*

REFERENCE: Edwards, J.M. and A. Slingo: Studies with a flexible new radiation code. I: Choosing a configuration for a large-scale model. Quart. J. Roy.Meteor. Soc., 122, 689-719, 1996.

p. 3447, L3: Please correct a position of the values “2” (power of root) in (B3).

Corrected

p. 3474, L2 in caption of Fig. A1: “ad Dome Concordia” -> “at Dome Concordia”

Corrected

1 Measurements and modelling of snow particle size and 2 shortwave infrared albedo over a melting Antarctic ice 3 sheet

4
5 R. Pirazzini¹, P. Räisänen¹, T. Vihma¹, M. Johansson¹, and E.-M. Tastula^{1,*}

6 [1]{ Finnish Meteorological Institute, Helsinki, Finland }

7 [*]{now at: College of Marine Science, University of South Florida, St. Petersburg, FL,
8 USA }

9 Correspondence to: R. Pirazzini (roberta.pirazzini@fmi.fi)

10 11 **Abstract**

12 The albedo of a snowpack depends on the single-scattering properties of individual snow
13 crystals, which have a variety of shapes and sizes, and are often bounded in clusters. From the
14 point of view of optical modelling, it is essential to identify the geometric dimensions of the
15 population of snow particles that synthesize the scattering properties of the snowpack surface.
16 This involves challenges related to the complexity of modelling the radiative transfer in such
17 an irregular medium, and to the difficulty of measuring microphysical snow properties. In this
18 paper, we illustrate a method to measure the size distribution of a snow particle parameter,
19 which roughly corresponds to the smallest snow particle dimension, from two-dimensional
20 macro-photos of snow particles taken in Antarctica at the surface layer of a melting ice sheet.
21 We demonstrate that this snow particle metric corresponds well to the optically equivalent
22 effective radius utilized in radiative transfer modelling, in particular when snow particles are
23 modelled with the droxtal shape. The surface albedo modelled on the basis of the measured
24 snow particle metric showed an excellent match with the observed albedo when there was
25 fresh or drifted snow at the surface. In the other cases, a good match was present only for
26 wavelengths longer than 1.4 μm . For shorter wavelengths, our modelled albedo generally
27 overestimated the observations, in particular when surface hoar and faceted polycrystals were
28 present at the surface and surface roughness was increased by millimetre-scale cavities
29 generated during melting. Our results indicate that more than just one particle metric

1 distribution is needed to characterize the snow scattering properties at all optical wavelengths,
2 and suggest an impact of millimetre-scale surface roughness on the shortwave infrared
3 albedo.

4

5 **1 Introduction**

6 The snowpack is composed of snow crystals (grains) more or less bounded with each other,
7 which have shapes and sizes that change during the metamorphism process. The boundaries
8 between grains are not always identifiable, and X-ray micro-tomography has revealed a much
9 more complex structure than usually described by a single grain size value and a
10 morphological description (Schneebeli and Sokratov, 2004). Nevertheless, the snow grain size
11 is a fundamental quantity used in radiative transfer modelling to characterize the scattering
12 properties of the snowpack and to determine its degree of metamorphism (Flanner and
13 Zender, 2006). As such, it is an essential parameter for the interpretation of the reflected
14 signals in optical and radar remote sensing, and it is used in the most sophisticated
15 simulations of snow surface albedo, snow mass and energy budget and length of melting
16 season, as well as in water runoff estimation and avalanche risk assessment.

17 The scattering properties of snow grains are wavelength dependent, and the impact of snow
18 layering on the surface reflectance varies according to the penetration depth of the considered
19 wavelength. Snow grain size variations have larger impact on the near-infrared (NIR, 0.7-1.0
20 μm) and shortwave infrared (SWIR, 1.0-2.5 μm) reflectance compared to the visible (VIS,
21 0.35-0.7 μm) reflectance (Wiscombe and Warren, 1980), because grains absorb more
22 radiation in the NIR and SWIR spectral regions. Thus, a selected NIR or SWIR wavelength,
23 or a combination of wavelengths, is utilized to retrieve snow grain size from in-situ or remote
24 sensing reflectance observations (Gallét et al., 2009; Kokhanovsky et al., 2011; Nolin and
25 Dozier, 2000; Painter et al., 2007).

26 The relationship between the snow surface reflectance and the shape and size distribution of
27 the snow grains is not trivial and not yet fully understood. Snow crystals of different shapes
28 and sizes coexist at the surface and in the sub-surface layers reached by the solar radiation.
29 Generally, variability in snow crystal size and shape is largest at the surface, which is the
30 layer that mostly contributes to the surface reflectance. In most radiative transfer models,
31 snow is represented with an optically equivalent “effective radius” (r_{eff}), which is the radius
32 of a collection of mono-disperse spheres having a total volume-to-surface area-ratio equal to

1 that of the true snow grain population (Grenfell and Warren, 1999). The hypothesis behind
2 this formulation is that the collection of spheres possesses the same scattering properties as
3 the physical snow grain population. Indeed, in the case of spheres and randomly-oriented
4 convex particles, the volume-to-surface-area equivalent radius (r_{VA}) coincides with the mean
5 radius of the particle ensemble weighted by the particle's projected area (r_{VP} , Cauchy, 1841),
6 which is directly proportional to the particle's scattering contribution (Hansen and Travis,
7 1974).

8 The equivalent sphere approximation has been extensively applied in the optical retrieval of
9 snow grain effective radius by using radiative transfer inversion algorithms which utilize the
10 measured radiance (Kokhanovsky et al., 2011; Lyapustin et al., 2009; Nolin and Dozier, 2000;
11 Painter et al., 2007; Scambos et al., 2007; Stamnes et al., 2007). As r_{VA} is directly related to
12 the snow specific surface area (SSA) through the relationship

$$13 \quad SSA = 3/\rho_{ice}r_{VA} \quad (1)$$

14 where ρ_{ice} is the ice density, measurements of SSA have been used to model the radiative
15 properties of snow (Carmagnola et al., 2013; Domine et al., 2006; Gallet et al., 2011). The
16 usage of SSA has its advantages: 1) the difficult identification of the single snow crystals is
17 not required, 2) SSA is an unambiguous and well defined quantity, 3) accurate measurement
18 methods are available (based on stereology, X-ray tomography, and gas-absorption), and 4)
19 fast, indirect optical measurement methods have recently been developed (Arnaud et al.,
20 2011; Berisford et al., 2013; Gallet et al., 2009). However, SSA (and r_{VA}) describes the
21 scattering property of the snow only in the case of convex grains. In the case of concave
22 grains, the volume-to-total surface area equivalent radius is less than the volume-to-projected
23 area equivalent radius: $r_{VA} < r_{VP}$.

24 Model calculations have shown that grains with the same optically equivalent radius but
25 different shapes result in different snow albedo (Jin et al., 2008; Mishchenko, 1999; Picard et
26 al., 2009). The impact of shape on the reflectance of a flat snow surface is particularly
27 profound for large solar zenith angle and wavelength due to the decreasing role of multiple
28 scattering and, thus, the increasing importance of the single scattering properties of the grains,
29 in particular the shape-specific phase function.

30 A large number of methods have been applied to measure the snow grain geometry. This is
31 due to the complex and laborious nature of these measurements, but also due to the

1 uncertainty on what is the most relevant dimension for the different applications (optical and
2 microwave radiative transfer, glaciological studies, avalanche forecasting). A snow grain is by
3 definition a single crystal (Fierz et al., 2009), but in many snow grain analyses there is no
4 distinction between single crystals and multi-crystals objects or aggregates (Aoki et al., 2000;
5 Gay et al., 2002). The “size” of a grain is defined as its greatest extension according to the
6 International Classification (Colbeck et al., 1990; Fierz et al., 2009), and the grain size of a
7 snow sample is the average size of its characteristic grains. However, this grain metric is not
8 suitable for optical applications: Mätzler (1997) and Neshyba et al. (2003) demonstrated that
9 the shortest grain dimension is proportional to r_{VA} , and there is also experimental evidence
10 that this dimension best represent the scattering properties of the snow grains (Grenfell et al.,
11 | 1981; Aoki et al., 2000, 2003, [2011](#)).

12 An implication of all these considerations is that extensive and detailed snow and albedo
13 observations are needed to establish the link between the snowpack microphysical
14 characteristics and surface albedo, and to verify the radiative transfer model assumptions in
15 snow-radiation interaction. Datasets including contemporary in-situ observations of albedo
16 and grain texture are few, in comparison with the large variety of existing snow conditions
17 (Aoki et al., 2000; Carmagnola, 2013; Domine et al., 2006; Nakamura et al., 2001; Painter
18 and Dozier, 2004). These datasets only include short measurement periods, as both spectral
19 albedo and snow observations rely on very laborious and time consuming methods.

20 In this study we analysed snow and albedo data collected in Dronning Maud Land, Antarctica,
21 in the austral summer 2009-2010. As we wanted to examine real snow particle dimensions,
22 shapes, and size distributions, we took two-dimensional (2D) macro-photos of snow grains.
23 More sophisticated and accurate methods to measure snow morphology (as 3D microscope
24 stereology, X-ray tomography, and gas absorption techniques) do exist, but we wanted to
25 explore the capability of a technically simpler method to obtain optically relevant snow
26 particle dimensions. The sampling procedure is particularly critical in all techniques
27 employed to measure the snow texture. Both direct and indirect methods disturb the target
28 sample in one way or another. In our case, the snow samples consisted of disaggregated snow
29 particles, some of which were single crystals and some multi-crystals and aggregated grains.
30 Hereafter, we adopt the term “particle” to indicate an observed single snow element, which
31 may or may not consist of a single crystal, and which is considered as a distinct optical
32 scatterer/absorber. In this study, we hypothesize that the shortest skeleton branch of the 2D

1 projection of the snow particle is a close approximation of the shortest particle dimension, and
2 we develop an objective method to obtain this metric from the 2D macro-photos (~~Pirazzini et~~
3 ~~al., in preparation~~). The advantage and interest of using 2D macro-photos to measure optical
4 particle size compared to the faster, indirect optical methods lie in the direct and independent
5 quantification of the snow particle metric distribution. 2D particle projections allow the
6 investigation of the impact of particle morphology and size distribution on the measured
7 albedo, and offer the possibility to extract more than one metric per particle distribution.
8 Indeed, we will demonstrate in this study that, in some cases, r_{oeff} and, consequently, the
9 appropriate particle metric, depend on wavelength. The main objectives of the present paper
10 are 1) to verify if the proposed particle metric (the shortest skeleton branch) synthesizes well
11 the scattering properties of the snowpack, and 2) to verify if the measured vertical profiles of
12 snow density and particle metric distribution give suitable and sufficient information to model
13 the surface albedo. The schematic diagram of Fig. 1 illustrates the flow of the work: particle
14 metric distributions were calculated from the snow images, and, together with the measured
15 snow density, were fed into the radiative transfer model DISORT (Discrete Ordinates
16 Radiative Transfer Program for a Multi-Layered Plane-Parallel Medium, Stamnes et al., 1988)
17 to calculate the corresponding surface albedo. The modelled spectral albedo was then
18 compared to the observations, and the particle effective radii derived from the particle metric
19 distributions were compared with the optical effective radii calculated from the observed
20 surface albedo. The structure of the paper is as follows: after describing the snow and
21 radiation datasets in Sect. 2, the methods utilized to analyse the data and to model the surface
22 albedo are presented in Sect. 3. Results are illustrated in Sect. 4 and further discussed in Sect.
23 5. In Sect. 6 the main results are summarized, and the conclusions drawn. To increase the
24 readability of the text, all the acronyms and symbols utilized in the various Sections are listed
25 in Table A1.

26

27 **2 Observations**

28 The snow particle size and radiation data analysed here were collected during the austral
29 summer 2009-2010 over an ice sheet near the Finnish Antarctic station Aboa (73°03'S,
30 13°25'W, ~200 m a.s.l.). The ice sheet was gently sloping (with a local inclination of about
31 0.5°) towards an ice shelf, the edge of which was approximately 130 km to the northwest. The
32 dataset includes measurements taken during two overcast and six clear-sky days (Table 1): in

1 the morning or around noon, vertical profiles of snow density, temperature, and particle
2 macro-photos were acquired from a snow pit. Surface spectral reflectance was measured in a
3 close-by undisturbed area, with a time difference from the snow pit measurements ranging
4 from 0.5 to 3.5 hours (Table 1).

5 **2.1 Meteorological conditions**

6 The shape and size of the near-surface snow particles are strongly affected by the current and
7 previous meteorological conditions. To interpret the snow particle observations, we calculated
8 the mean and standard deviation of the air temperature T_a (at the height of 3.5 m), air relative
9 humidity (2.4 m), as well as wind speed and direction (10 m) for the time frame covered by
10 the snow pit and reflectance measurements (Table 1). In addition, we report in Table 1 the
11 mean, minimum, and maximum T_a in the 24-hour period preceding the snow particle
12 observations. The humidity and wind values are based on measurements at an Aanderaa
13 weather mast. The weather mast data on air temperature included, however, errors due to
14 sensor heating by reflected solar radiation (the radiation shields were not protective enough
15 for radiation reflected from the surface). Hence, we calculated the air temperature from sonic
16 anemometer measurements, which are not affected by radiation. The temperature that a sonic
17 anemometer yields is within about 0.20% (0.5 °C) of the virtual temperature, which we
18 converted to the true air temperature following Sjöblom and Smedman (2002). Both the
19 weather mast and sonic anemometer were located within 200 m of the snow measurement
20 site. The air temperature remained below 0 °C during all days except 5 January, when the
21 wind was from the Basen nunatak, where the rocky surface was strongly heated by clear-sky
22 solar radiation. During all examined cases wind was generally light or gentle. Assuming that,
23 in case of dry snow at the surface, the threshold wind speed at the height of 0.5 m for the
24 occurrence of snowdrift was 6 ms⁻¹, the longest lasting (about 18 hours) snowdrift episode
25 occurred between the midday of 23 December and the morning of 24 December, while shorter
26 lasting (a few hours) episodes occurred on 28 and 29 December. Later during the campaign,
27 the surface melting taking place before or during the high wind episodes prevented the
28 snowdrift. Light snowfall occurred on 22 and 23 December, and on 1, 8, 13, 17 and 18
29 January, but the amount of precipitation was not recorded. The 24 hours preceding the snow
30 observations in the two overcast cases (23 December and 14 January) were characterized by
31 overcast conditions and small T_a excursions (2.9 and 3.8 °C, respectively). The largest T_a
32 excursion (9.2 °C) was recorded in the 24 hours preceding the clear-sky case of 26 December,

1 mostly due to the strong nocturnal cooling (T_a minimum was -13.4 °C). Later in the season,
2 the nocturnal cooling was less pronounced (T_a minimum was between -9.1 and -5.7 °C).

3 **2.2 Snow density and temperature**

4 Similarly to our campaigns in 2006-2007 and 2007-2008 (Vihma et al., 2011), snow
5 temperature and density profiles were measured in the uppermost 50 cm of the snow pits, but
6 here we only present and utilize data from the uppermost 20 cm. Snow temperature (T_{snow})
7 was measured at the surface and at the depths of 2.5, 5, 10, 15, and 20 cm with the handheld
8 temperature probe Ebro TFX 410, which is equipped with a 30 cm probe and has a nominal
9 accuracy of ± 0.3 °C. The vertical snow density (ρ_{snow}) profiles were measured with a steel
10 cylinder (volume 247 cm³) pushed horizontally in the snow pit wall. The cylinder has a
11 diameter of 5 cm, and snow samples were taken with the centre of the cylinder at the depths
12 of 5, 10, and 20 cm. ρ_{snow} in the uppermost 2 cm was measured using a small aluminium box
13 (48 cm³, $\sim 5 \times 5 \times 2$ cm). The samples were weighted using a digital balance with an accuracy of
14 0.002 kg. For each snow pit, two vertical profiles of temperature and density were measured,
15 within approximately 40 cm of each other, in a time interval of about 15 minutes. In our
16 analyses and model simulations of the surface albedo, we utilized the mean of the two vertical
17 profiles of ρ_{snow} and T_{snow} for each snow pit, and we estimated their uncertainty as the square
18 root of the sum of the squares of instrumental error and intra-pit variability (Table 2). We
19 define the intra-pit variability as twice the intra-pit standard deviation of density and
20 temperature based on all the snow pits measured during the campaign (45 and 47 snow pits
21 for temperature and density, respectively).

22 In addition to the intra-pit variability, snow density and temperature varied also at larger
23 horizontal scales, as detected via measurements at 10-m-intervals along a 100-m-long line, on
24 six days for density and eight days for temperature. The standard deviation of density in the
25 uppermost 2 cm was largest (87 kg m⁻³) on 26 December, after the snow redistribution
26 associated to the snowdrift event of 23-24 December, and smallest (38 kg m⁻³) in the
27 afternoon of 19 January after a period of strong melt. The standard deviation was large (72 kg
28 m⁻³) also on 14 January after a precipitation event. Horizontal variations in snow surface
29 temperature were largest in cold conditions (standard deviation 0.4 °C) and naturally very
30 small during melt. For snow density, the standard deviation strongly decreased with depth,

1 whereas for snow temperature it remained rather constant in the uppermost 20 cm, which was
2 the case also at the intra-pit scale (Table 2).

3 Figure 2 shows the mean snow pit T_{snow} and ρ_{snow} profiles for the eight analysed cases. The
4 warming of the snowpack during the progress of the summer is clearly evident, with a marked
5 melting and an almost vertically constant profile at 0 °C in the last three analysed days (Fig.
6 2a). The ρ_{snow} profiles show a progressive compaction of the snowpack for most of the layers,
7 but not for the surface. Particularly on 14 and 19 January, during the strong melting, ρ_{snow} was
8 much lower at the surface than in the underlying layers (Fig. 2b). The highest ρ_{snow} exceeding
9 500 kg m⁻³ were due to the presence of ice layers formed via refreezing of meltwater; such
10 high ρ_{snow} values were not observed during our previous campaigns at the same site in 2006-
11 2008, when the summers were colder (Vihma et al., 2011).

12 **2.3 Near-surface snow stratigraphy**

13 Stratigraphy observations were only made at a qualitative level, without snow hardness
14 measurements and systematic recording of layer properties. However, the collected
15 information provided a useful picture of the evolution of the uppermost snowpack layers. For
16 most of the measurement period, the snow surface was very hard. On 23 December the
17 surface was covered with a mixture of small rounded particles ([code RGsr](#), greatest extent of
18 0.2-0.5 mm), faceted rounded particles ([code RGxf](#), greatest extent of 0.5-1 mm), and
19 aggregates ("[Agg](#)", greatest extent of 1-1.5 mm). Moreover, a thin (0.1-0.2 cm) ice layer was
20 present at 10 cm depth. At 5 cm depth, rounding faceted particles of various sizes ([code FCxr](#),
21 greatest extent of 0.2-2 mm) were present. On the morning of 26 December a wind-packed
22 surface crust covered with very fine rounding faceted particles (greatest extent of 0.1-0.6 mm)
23 was observed, both at the surface and at 5 cm depth. Ice layers were present at the depths of 8
24 and 10 cm. From 28 December to 3 January, the uppermost 2 cm layer was refrozen both in
25 the morning and evening observations. Although surface snow temperature started reaching
26 0°C only on 1 January, subsurface melting due to absorption of solar radiation likely occurred
27 also in the previous days, as for instance in the 24 hours before the clear-sky case of 29
28 December, when maximum T_a was -3.0 °C. On 29 December, rounded particles ([code RGlR](#),
29 greatest extension of 0.2-0.8 mm) and rounded irregular polycrystals ([code MFpc](#), greatest
30 extension of 1-3 mm) extended from the surface to the depth of 5 cm ([the surface appearance](#)
31 [on 29 December is shown in Fig. 3a](#)). With the progress of the melting, the refrozen layer at

1 the top extended to the depth of 15 cm in the evening of 5 January, and to the depth of 20 cm
2 | in the evening of 13 January. On 5 January, a mixture of thin faceted particles ([code FCsf](#),
3 | greatest extent of 0.1-0.5 mm), rounding faceted polycrystals and rounding surface hoar
4 | ([code SHxr](#)) having greatest extension of 1-2 mm and thin protrusions of 0.05-0.3 mm
5 | diameter was present at the surface (Fig. 3b). By 7 January they extended to the uppermost 5
6 | cm, forming a highly porous but still hard layer (at least when air temperature was below
7 | 0°C). In the following days, the surface roughness at the centimetre and millimetre scale
8 | increased, more as a result of the undergoing snow metamorphism than due to the action of
9 | the wind (which was generally light). In the morning of 12 January, after a clear-sky night,
10 | striated, sharp-edged surface hoar ([code SHsu](#), greatest extent of 1-1.3 mm)~~s~~ was present at
11 | the surface, together with rounded polycrystals having greatest extent of 1-2 mm and small
12 | protrusions of 0.05-0.2 mm diameter. At the 5 cm depth, the particle population was a mixture
13 | of rounded polycrystals (greatest extent of 1-2.5 mm) and rounded particles (greatest extent of
14 | 0.2-0.7 mm). After the snowfall on 13 January, the surface was smoothed and the concavities
15 | were filled by fine, irregular snow crystals ([code PPIr](#)). Starting on 14 January, the coarse
16 | grains forming the 0-5 cm layer became gradually looser, and the snow layer softened. On 14
17 | January faceted polycrystals (greatest extension of 1-2 mm) together with partly decomposed
18 | precipitation particles ([code DFdc](#), greatest extent of 0.1-0.5 mm) were observed at the
19 | surface. On 18 January, a light snowfall refreshed and smoothed again the snow surface (Fig.
20 | 3c), and on 19 January columns [and needles](#) (greatest extent of 0.2-0.7 mm)~~, needles, and~~
21 | [together with](#) rounding faceted polycrystals (greatest extent of 1-2 mm) were present at the
22 | surface. [A summary of the size and shape characteristics of the surface snow particles is given](#)
23 | [in Table 3.](#)

24 **2.4 Snow particle samples**

25 To ensure the possibility of photographing snow particle samples in all temperature, wind,
26 and illumination regimes, we dug a 2-m deep cave in the snowpack. The bottom of the cave
27 was at a constant temperature of about -7°C. A wooden plate covered the cave, sheltering it
28 from wind and solar radiation (Fig. 4a). To photograph the snow particles, during each snow
29 pit excavation a block of snow including the surface layer down to the depth of 30-40 cm was
30 extracted and transported in the nearby snow cave. To extract the snow particles from the
31 block, we brushed the snow surface with a thin and flexible steel palette knife, detaching the
32 snow particles from the background snowpack texture. Particles were collected on a slide

1 glass, which was then placed in a holder attached to the camera support system (Fig. 4b). We
2 tried to avoid contact and overlapping between particles, often resampling the particles
3 several times, in order to facilitate the segmentation during the image processing (see Sect.
4 3.1.1). We did not screen out either crystal fragments or natural clusters of grains, as we
5 wanted to include also these particles in our analysis. The particles were illuminated from
6 below, with a bulb covered by a thick layer of white polyethylene foam to diffuse the light
7 and prevent the heating of the glass. Macro-photos were taken with a Canon EOS 450D
8 digital camera equipped with a 60 mm macro lens and a 68 mm extension tube.

9 **2.5 Snow nadir reflectance**

10 Snow spectral reflectance (in the range 0.35-2.5 μm) was measured with an ASD FieldSpec
11 JR spectroradiometer manufactured by Analytical Spectral Devices, Inc. (hereinafter referred
12 to as ASD), now PANalytical. The ASD has three sensors covering three distinct spectral
13 regions: visible and near-infrared (VNIR, 0.35-1.0 μm), shortwave infrared 1 (SWIR1, 1.0-
14 1.83 μm), and shortwave infrared 2 (SWIR2, 1.83-2.5 μm), with a spectral resolution between
15 3 and 10 nm. Snow relative reflectance was obtained from the ratio of the snow radiance to
16 the reference radiance, reflected from an almost-Lambertian Spectralon target-white panel.
17 The relative reflectance was then multiplied with the calibration data of the reference panel to
18 get the absolute snow spectral reflectance. Snow and reference radiances were acquired using
19 the ASD bare fore optic (with a nominal field of view of 25°) pointing toward nadir, and both
20 of them were consecutively measured 30 times. The acquisition time of the 60 spectra was
21 about 6 minutes. The spectrum of snow relative reflectance was calculated using the average
22 of the 30 snow spectra and the reference spectrum. The bare fore optic was mounted on a
23 tripod at about 1 m height above the surface; therefore the footprint area of the
24 spectroradiometer was a circle with a radius of about 22 cm. During clear-sky days,
25 measurements were taken from 1 to 4 times, when the solar zenith angle (θ_0) was between 50°
26 and 60° . Apart from instrumental inaccuracy, potential error sources of the spectral
27 reflectance measurement include variations in incident solar irradiance during the
28 measurement time and deficiencies in the measurement method, which are discussed below.

29 For a correct measurement of the reference radiance, the reference Spectralon panel should be
30 horizontally aligned, and should completely cover the 25° field of view of the bare fore optic.
31 Thus, the 12.5x12.5 cm wide reference panel should be placed at a distance smaller than 28.2
32 cm from the bare fore optic and centred on its vertical projection. In our experiment, the

1 horizontal levelling was checked through a bubble balancer, and the plate was manually held
2 about 20 cm below the fore optic. However, the centring with respect to the vertical
3 projection of the fore optic was done only visually (and, therefore, approximately). A first
4 analysis of the data revealed a large positive bias in the VNIR snow reflectances, with a step-
5 like drop of reflectance at the 1000 nm junction. We concluded that the reference panel did
6 not completely cover the effective field-of-view (FOV) of the VNIR spectrometer, which is
7 larger than the nominal FOV value given by the manufacturer (Mac Arthur et al., 2011). We
8 therefore rejected all data at wavelengths smaller than 1000 nm, and limited our analysis to
9 the SWIR spectrum.

~~10 The horizontal levelling of the reference panel was checked with a bubble balancer. The
11 uncertainty of snow reflectance related to the horizontal levelling of the reference panel (σ_{θ_0})
12 was $\pm 3\%$ ($\pm 4\%$) in the SWIR1 (SWIR2) wavelength region, estimated as the normalized
13 standard deviation of 30 consecutive spectra of reference reflectance.~~

14 The small footprint area of the spectrometer on one hand ensured that the shadows of the
15 instrument setup and of the operator did not reach the target surface, but on the other hand
16 amplified the impact of the possible roughness features and slopes on the measurements
17 performed under clear skies (Pirazzini, 2004). A surface area as smooth as possible was
18 chosen for each reflectance measurement, but the measured spot changed every time, as the
19 surface needed to be undisturbed by previous measurements, and the chosen spots were often
20 located over gentle dunes, which were free from roughness features (Fig. 3). Thus, a part of
21 the difference between the measurements is most probably attributable to differences in the
22 local slope. The surface tilting over these gentle snow dunes was very modest, usually
23 between 0.5° and 2° . As we did not measure the surface tilting and its direction at each
24 measurement spot, we calculated the surface tilting uncertainty applying equation (4) of
25 Grenfell et al. (1994) assuming a tilt of 2° and that the Sun was always in the uphill or
26 downhill direction, maximizing the negative and positive errors respectively (Fig. 5). The
27 estimated maximum error due to surface tilting (Δ_{tilt}) was therefore only a function of θ_0 ,
28 ranging between $+6\%$ ($+8\%$) in the downhill direction ($\Delta_{tilt,down}$) and -2% (-4%) in the uphill
29 direction ($\Delta_{tilt,up}$) at $\theta_0 = 50^\circ$ (60°).

30 The spread of the 30 consecutive snow reflectance spectra can evidence the possible change
31 in solar illumination during the time interval of three minutes (revealing, for instance, the
32 possible presence of thin cirrus in the solar direction). The repeatability error of the snow

1 | reflectance ($\sigma_{r_{ept}}$) was calculated as the normalized standard deviation of reflectance among
2 | the 30 spectra. Excluding three wavebands with a very low signal to noise ratio (1.33-1.6 μm ,
3 | 1.8-2.1 μm , and 2.3-2.5 μm), $\sigma_{r_{ept}}$ was within $\pm 0.6\%$ ($\pm 1.5\%$) in the SWIR1 (SWIR2)
4 | wavelength region in most of the clear-sky cases, and within $\pm 2.0\%$ ($\pm 4.0\%$) on 5 and 6
5 | January, where some thin cirrus were present, and during overcast conditions. These
6 | repeatability errors are consistent with the $\pm 2\%$ ASD repeatability error found in well
7 | controlled laboratory and field experiments (Kuester et al., 2001) and in measurements of
8 | snow radiance over the Antarctic plateau (Hudson et al., 2006).

9 | The repeatability error of the reference reflectance (σ_{ref}), calculated as the normalized
10 | standard deviation of 30 consecutive spectra of reference reflectance, was $\pm 3\%$ ($\pm 4\%$) in the
11 | SWIR1 (SWIR2) wavelength region. This uncertainty is larger than $\sigma_{r_{ept}}$, and is presumably
12 | attributable to the inaccuracy of the manual horizontal levelling of the Spectralon plate.

13 | Lastly, a possible error that is difficult to quantify is related to the presence of the operator.
14 | While the operator was always positioned opposite to the Sun's direction and therefore did
15 | not cast a shadow on the footprint area of the spectroradiometer, his presence caused a small
16 | reduction of the diffuse radiation reaching the area. In some cases the operator was closer to
17 | the reference panel than to the target area, causing a possible overestimation of the snow
18 | reflectance. Since in most days we measured several spectra a few hours apart, as a final
19 | quality criterion for our reflectance spectra, we selected only those spectra that lied in the
20 | range of uncertainty of the other spectra collected on the same day. A total of three spectra
21 | were discarded with this criterion. The analysed spectra that fulfilled all quality criteria and
22 | were temporally closest to the snow pit measurements are listed in Table 1.

23 | **2.6 Sky spectral irradiance**

24 | Before each set of reflectance spectra, 30 consecutive spectra of downward irradiance were
25 | collected, with the ASD cosine receptor fore optic pointing toward the zenith. These data
26 | were utilized to calculate the broadband surface albedo and the surface net shortwave
27 | radiation in Sect. 4.2. Excluding the wavebands with very low signal to noise ratio (see Sect.
28 | 2.5), the series of 30 consecutive spectra were overlapping within $\pm 0.5\%$ in clear-sky
29 | conditions and $\pm 0.7\%$ and $\pm 2.4\%$ in overcast conditions in the VNIR and SWIR regions,
30 | respectively. The cosine receptor utilized for the solar irradiance measurements does not have
31 | a perfect cosine response. For θ_0 between 50° and 60° , the deviation of the cosine receptor

1 from the pure cosine response is about +10% in the VNIR region and lower than +2% in the
2 SWIR region (Carmagnola et al., 2013; Lubin and Vogelmann, 2011). Thus, the total error in
3 the measured solar irradiance was in the range -1 to +10% in the VNIR region, and in the
4 range -1 to +2% (-2 to +2%) in the SWIR region during clear-sky (overcast) conditions.

5

6 **3 Methods of data analysis and modelling**

7 The content of Sections 3 and 4 can be summarized as follows (see also Fig. 1): from the
8 processing of the snow particle macro-photos (Sect. 3.1) we obtained the vertical profiles of
9 the particle metric distribution. These, together with the vertical profiles of ρ_{snow} , were used as
10 input of the radiative transfer model DISORT to calculate the snow surface spectral albedo
11 (Sect. 3.3). The surface albedo was also obtained from the measurements of surface nadir
12 reflectance and a parameterization of the snow anisotropic reflectance factor (Sect. 3.2), and
13 was used to validate the DISORT-derived surface albedo (Sect. 4.1). The broadband albedo
14 and net shortwave radiation obtained from the measured and modelled spectral albedo were
15 compared in Sect. 4.2. DISORT was then applied to the calculation of the optically equivalent
16 particle radius r_{oeff} based on the reflectance-derived spectral albedo, and the results were
17 validated against the effective particle radius obtained from the metric distributions (Sect.
18 4.3). Finally, the sensitivity of r_{oeff} to ρ_{snow} and to the effective variance of the particle metric
19 distribution (defined in Sect. 3.1.3) was explored (Sect. 4.4).

20 **3.1 Snow particle macro-photos**

21 **3.1.1 Image enhancement and segmentation**

22 The original colour images had a resolution of 4272x2848 pixels for each of the three colour
23 planes. The image processing was done applying the Matlab software. To improve the
24 detection of the particle contour (image segmentation) two series of bi-cubical interpolation
25 were applied (in each interpolation, each pixel resulted from the weighted average of the 4
26 neighbouring pixels in both x and y axes). This caused an image reduction of 1:4 leading the
27 final images to have 1078712x7121078 pixels. The images were then converted to grayscale
28 followed by contrast adjustment and sharpening.

29 When choosing the image segmentation method, the general guideline that we followed was
30 to obtain a black and white mask that is as faithful as possible to the image segmentation

1 performed by the human brain. It is well known that human eyes and brain can segment an
2 image better than any artificial intelligence. In order to achieve a sufficiently accurate result,
3 we developed a segmentation procedure that requires a human control, as previously done by
4 Pringle et al. (2009). The images were converted to binary black and white (*bw*) masks
5 through two edge detection algorithms (one based on the Sobel method, and the other based
6 on a threshold luminance). The detected snow particles in the two binary masks were then
7 dilated, the interior gaps were filled, and finally the snow particles were smoothed out to the
8 original size. To allow reasonable image quantification, snow particles composed of less than
9 20 pixels were eliminated, and all snow particles connected to the edge of the image and
10 therefore not entirely included in the image were automatically masked out.

11 The key step of this image processing procedure is the choice of the proper settings. For each
12 image, the combination of the allowed settings (contrast adjustment, edge detection algorithm,
13 gray threshold, dilation/erosion radius, minimum number of pixels per detected particle) that
14 generated the *bw* mask closest to the visual segmentation was chosen. The manual setting of
15 the parameters can introduce a certain level of subjectivity in the analysis, discussed in
16 Section 3.1.3. The false snow particles (i.e. water droplets or dirtiness detected as snow
17 particles) and misrepresented snow particles (in shape or size) that occasionally still remained
18 in the final mask were singularly removed. Figure 6a shows an example of a segmented
19 image.

20 An artefact of the particle detection method is that snow particles very close to each other
21 were not distinguished and were identified as single particles. However, the biggest clusters
22 were often connected to the border and were therefore automatically eliminated. The
23 magnification was not adjusted for each image; therefore, the samples characterized by small
24 particles contained a larger population than the samples with large particle sizes. This has an
25 impact on the representativeness of the samples (see Sect. 3.1.3), which is higher for
26 populations of small snow particles.

27 3.1.2 Image quantification and definition of particle metric

28 The final images contained the 2D projections of the sampled snow particles, with an image
29 resolution (i.e., pixel size) that varied between 0.008 mm and 0.014 mm. For each particle, we
30 determined the skeleton by successively removing pixels on the boundary, without letting the
31 particle to break apart (using the automatic routine "bwmorph" of the Matlab Image

1 Processing Toolbox). Endpoints and branch points were then identified as the extremities and
 2 the junction nodes of the skeleton branches, respectively (Fig 6b). We—calculated the
 3 lengths of skeleton branches as the Euclidean distances between the skeleton’s endpoints and
 4 their nearest branch points ~~(the junction nodes of the skeleton’ branches)~~, and we selected the
 5 shortest skeleton branch (*SSK*) as the particle metric (Fig. 6b). In practice, we expect *SSK* to
 6 be a close approximation of half the width of the shortest particle dimension, which has
 7 shown the best match with $r_{o\text{eff}}$ (Aoki et al., 1998, 2000, 2003).

8 The number and location of the skeleton’s endpoints is affected by the image segmentation:
 9 smoother contours result in fewer endpoints while edged contours produce more of them.
 10 However, the settings in the image processing procedure were adjusted so that shape and
 11 contour distortions were minimized, or badly contoured particles were eliminated. Endpoints
 12 are also affected by how well the details of shape are resolved in the digital photo. If the
 13 image resolution is lower than the dimension of the particle details, the location and the
 14 number of endpoints will be erroneous. In our case, the final resolution was of the same order
 15 of magnitude as that of the smallest possible snow particle dimension (Liou et al., 2008);
 16 therefore we believe that the endpoints were rather well identified.

17 3.1.3 Effective radius and effective variance of the particle metric distribution

18 One objective of our study is to relate the particle metric distributions obtained from the
 19 macro-photos to the $r_{o\text{eff}}$ derived from the surface spectral albedo. For radiative transfer
 20 calculations, Hansen and Travis (1974) defined the effective radius r_{eff} of an ensemble of
 21 spheres as the area-weighted mean radius of the distribution of scattering particles:

$$r_{\text{eff}} = \frac{\sum r_i^3}{\sum r_i^2} \quad (2)$$

22 where r_i is the radius of the i^{th} particle. This concept rose from the consideration that each
 23 particle scatters an amount of light proportional to its geometric cross-sectional area (i.e.,
 24 projected area). Furthermore, as a measure of the width of the size distribution, the effective
 25 variance v_{eff} was defined as (Hansen and Travis, 1974; Chýlek et al., 1992):

$$v_{\text{eff}} = \frac{\sum [(r_i - r_{\text{eff}})^2 r_i^2]}{r_{\text{eff}}^2 \sum r_i^2} = \frac{m_4 m_2}{m_3^2} - 1, \quad (3)$$

26 where m_2 , m_3 , and m_4 are the second, third, and fourth moments of the particle size
 27 distribution. For our measured *SSK* distributions, we calculated r_{eff} and v_{eff} by interpreting r_i in

1 Eqs. (2) and (3) as the dimension of the i^{th} particle according to the *SSK* metric.

2 3.1.4 Uncertainties in measured particle metrics

3 Throughout this paper, uncertainty in r_{eff} and v_{eff} (and albedo) is estimated in terms of the
4 “5% and 95% errors” (E05 and E95, respectively). The 5% (95%) error is defined as the
5 difference between the lower (upper) limit of the 90% confidence interval and the best
6 estimate. We consider here two sources of errors in the obtained *SSK* distributions: one due to
7 the subjective choice of the setting parameters in the image segmentation procedure, and the
8 other due to the representativeness of the measured samples.

9 To estimate the first uncertainty, the segmentation procedure was applied by three different
10 persons (two of whom without any previous experience on image processing) on a subset of 3
11 samples. The “subjectivity errors” of the r_{eff} and v_{eff} obtained from the metric distributions
12 were calculated as the relative root-mean-square difference between the metric obtained by
13 one experienced and two unexperienced persons in image processing. The 5% and 95%
14 subjectivity errors applied to all studied cases (E05_{sub} and E95_{sub}, respectively) were
15 estimated by averaging the errors of the two unexperienced persons over the three sampled
16 cases and multiplying by the coefficient $c=1.6456$ (see also Appendix [AB](#)).

17 The “representativeness errors” indicate how well the measured samples represent the real
18 distribution of snow particles in the field. Each of our snow samples included a different
19 numbers of snow particles, ranging from about 40 (in case of very large particles) to some
20 hundreds (in case of small particles). Assuming that the measured samples are random and
21 unbiased, the uncertainty related to the limited population can be calculated using bootstrap
22 resampling. For each sample, we generated ten thousand random realizations of the original
23 distribution. Depending on whether the error in r_{eff} or v_{eff} was considered, the realizations
24 were ordered according to their r_{eff} or v_{eff} , and the values of r_{eff} or v_{eff} corresponding to the 5th
25 and 95th percentile of the population were used to define the respective 5% and 95% errors
26 (E05_{rpr} and E95_{rpr}).

27 The total uncertainty on the metric distributions (in the form of 5% and 95% errors) is given
28 by the square root of the sum of the squared subjectivity and representativeness errors.

1 3.2 Surface spectral albedo

2 In this study, we utilize the measured snow nadir reflectance to verify the reflectance
3 simulated by a radiative transfer model that applies the snow observations (particle size
4 distribution and density). We also derive the optical effective radius $r_{o\text{eff}}$, which will be
5 compared with the r_{eff} obtained from macro-photos. In general, $r_{o\text{eff}}$ can be obtained from the
6 snow reflectance at specific wavelengths/wavebands and viewing angles, measured from
7 remote sensing or in-situ sensors (e.g. Kokhanovsky et al., 2011; Painter et al., 2007).
8 Alternatively, the snow spectral albedo α (i.e. the reflectance integrated over the hemisphere)
9 is used, as in the case of the DUFISSS (Gallet et al, 2009) or ASSSAP (Arnaud et al., 2011)
10 instruments. We chose to use α , as it is more directly applicable to surface energy budget
11 calculations than the reflectances.

12 To get α , we divided the measured I_n by the anisotropic reflectance factor (Φ), which was
13 extracted from the measurements of Hudson et al (2006) at Dome Concordia, over the
14 Antarctic Plateau. The applied procedure is described in detail in Appendix [AB](#). The 5% and
15 95% errors of α introduced by the parameterization of Φ ($E05_{\Phi}^2$ and $E95_{\Phi}^2$, respectively) were
16 $\pm 7\%$. The total 5% and 95% errors of α calculated according to Eqs. ([AB1](#)) and ([AB2](#)) in
17 Appendix [AB](#) and averaged over the examined cases are listed in Table [43](#).

18 3.3 Modeling strategy

19 For comparison with the measurements, spectral surface albedos were computed using
20 DISORT (Stamnes et al. 1988), with 32 streams and δ -M-scaling (Wiscombe 1977) included.
21 Two snow crystal shape assumptions were considered: (1) spheres, and (2) severely
22 roughened (SR) droxtals. Droxtals are polyhedra with 20 faces, whose single-scattering
23 properties (*SSPs*) have been found to well represent the small ice crystals in clouds (Yang et
24 al., 2003). The *SSPs* of spheres (extinction efficiency Q_{ext} , single-scattering albedo ω (or co-
25 albedo $1-\omega$), and asymmetry parameter (g) were computed using Mie theory (Bohren and
26 Huffman 1983), while for droxtals, the database of Yang et al. (2013) was used. In both cases,
27 the refractive index of ice is based on Warren and Brandt (2008).

28 While spheres have been frequently used in radiative transfer applications involving snow, it
29 is well known that they do not represent well the *SSPs* of non-spherical particles such as
30 snow grains. A common feature for most non-spherical shapes, including SR droxtals, is that
31 sideward scattering is stronger than for spheres, and therefore, the asymmetry parameter g is

1 smaller. In fact, out of the non-spherical shapes considered by Yang et al. (2013), droxtals
 2 have the second lowest g (after aggregates of columns). Furthermore, the value of g for
 3 droxtals agrees closely with measurements conducted for blowing snow at $\lambda=0.8 \mu\text{m}$
 4 (Räisänen et al. 2015). This makes droxtals a reasonable first guess when representing the
 5 effects of snow grain non-sphericity on snow albedo. It is, however, clear that the observed
 6 shapes of snow grains rarely resemble droxtals (or any other single idealized shape), and
 7 therefore, the present calculations should rather be viewed as a sensitivity test than as a
 8 rigorous treatment of snow grain non-sphericity.

9 The behaviour of g and $1-\omega$ for spheres and droxtals is compared in Fig. 7 for the wavelength
 10 range $\lambda=1.0\text{-}2.5 \mu\text{m}$ considered in this study. Indeed, g is considerably smaller for SR droxtals
 11 than for spheres especially at relatively weakly absorbing wavelengths (e.g, $g\approx 0.78$ vs. $g\approx 0.89$
 12 at $\lambda=1.0 \mu\text{m}$), while $1-\omega$ is slightly larger for droxtals. Figure 7 also shows how both g and $1-$
 13 ω increase with increasing snow particle size, which explains the well-known fact that snow
 14 albedo decreases with increasing particle size. Due to their smaller g , for a given snow
 15 particle size, snow albedo is higher when droxtals rather than spheres are used to represent the
 16 SSPs. Equivalently, a larger snow particle size is needed for droxtals than for spheres to fit the
 17 observed albedo.

18 When modelling surface albedo, snow is considered pure, as soot concentration in Antarctica
 19 is so low as to be optically insignificant (Warren and Clarke, 1990). Moreover, the r_{eff}
 20 obtained from the SSK metric distribution is interpreted as the volume-to-projected area
 21 equivalent radius r_{VP} of either spheres or droxtals. The optical properties of a snow layer with
 22 density ρ_{snow} and thickness Δz , that is, the optical thickness τ and layer-mean single-scattering
 23 albedo $\bar{\omega}$ and asymmetry parameter \bar{g} , are computed through summation over the observed
 24 discrete particle size distribution:

$$25 \quad \tau = \rho_{\text{snow}} \Delta z \frac{\sum_i Q_{\text{ext}}(r_i) \pi r_i^2}{\rho_{\text{ice}} \sum_i 4/3 \cdot \pi r_i^3}, \quad (4)$$

$$26 \quad \bar{\omega} = \frac{\sum_i Q_{\text{ext}}(r_i) \omega(r_i) \pi r_i^2}{\sum_i Q_{\text{ext}}(r_i) \pi r_i^2}, \quad (5)$$

$$g = \frac{\sum_i Q_{\text{ext}}(r_i) \omega(r_i) g(r_i) \pi r_i^2}{\sum_i Q_{\text{ext}}(r_i) \omega(r_i) \pi r_i^2} \quad (6)$$

Here, $\rho_{\text{ice}} = 916.7 \text{ kg m}^{-3}$ is the density of pure ice, and $Q_{\text{ext}}(r_i)$, $\omega(r_i)$ and $g(r_i)$ are the extinction efficiency, single-scattering albedo and asymmetry parameter of a sphere or a droxtal with $r_{VP} = r_i$. Wavelength dependence is not marked explicitly. In addition to the calculations using the observed size distributions, some calculations using either a mono-disperse or lognormal size distribution are performed. In fact, the exact shape of the size distribution has little impact insofar the effective radius and effective variance are fixed (Chýlěk et al., 1992; Hansen and Travis, 1974).

In all the calculations reported here, the Henyey-Greenstein (1941) approximation is used for the scattering phase function. ~~On one hand, it is unlikely that droxtals (let alone spheres) would represent the phase function of snow particles accurately, and on the other hand, for the intermediate solar zenith angles considered here ($\theta_0 \approx 50^\circ - 60^\circ$), the Henyey-Greenstein phase function and the full phase function give quite similar results for snow albedo, with differences generally well below 0.01. On one hand, based on comparisons with a measured phase function for blowing snow (Räisänen et al. 2015), it is unlikely that droxtals (let alone spheres) would represent the phase function of snow particles accurately. On the other hand, in line with the findings of Boucher (1998) for aerosol radiative forcing (Fig. 6 in that paper), the differences in snow albedo computed with the full phase function and the Henyey-Greenstein phase function are small at the intermediate solar zenith angles ($\theta_0 \approx 50^\circ - 60^\circ$) considered here (in fact, generally below 0.01 for both droxtals and spheres).~~ Finally, out of the eight days considered, the incoming radiation at the surface is assumed to be diffuse for the two overcast days (23 Dec and 14 Jan) while for the other (cloud-free) days, parallel solar radiation is assumed.

The calculation of r_{eff} was done by applying the surface albedo spectra (described in Sect. 3.2), the measured ρ_{snow} (described in Sect. 2.1), and the v_{eff} of the SSK metric distribution. The sensitivity of the modelled r_{eff} to ρ_{snow} and v_{eff} is discussed in Sect. 4.3.

In order to facilitate the interpretation of our results, we estimated with DISORT the depths at which the snowpack is optically semi-infinite, in the range of analyzed wavelengths (1.0-2.5 μm). In particular, following Zhou et al. (2003) we calculated the snow depths required for

1 the albedo to reach 90% and 99% of the semi-infinite albedo (called 90% and 99% cutoff
2 depths, respectively). Figure 8 shows the spectral 90% (left panel) and 99% (right panel)
3 cutoff depths in the SWIR region for diffuse incident radiation, applying a snow density of
4 400 kg m^{-3} . The cases of the effective particle radius of 0.03, 0.1, 0.3, and 1 mm are
5 illustrated for the assumption of spherical shapes (continuous lines) and droxtal shapes
6 (dashed lines). Figure 8 reveals the progressive decrease of cutoff depths with increasing
7 wavelength, as observed in Zhou et al. (2003): for the intermediate particle radii considered
8 here (0.1 and 0.3 mm), the 90% cutoff depth is $\sim 3\text{-}10$ mm at the shortest SWIR, and becomes
9 less than 1 mm at the longest SWIR. In the case of near-surface density around 200 kg m^{-3} as
10 observed on 19 Jan (Figure 2b), the cutoff depths are double compared to the values shown in
11 Fig. 8. In all cases, even the 99% cutoff depth does not exceed 5 cm, and therefore, we
12 limited our analyses to the snow properties observed in the uppermost 5 cm.

13

14 **4 Results**

15 **4.1 Spectral albedo obtained from reflectance measurements and calculated** 16 **on the basis of the SSK metric**

17 Figure 9 illustrates, for the eight case studies, the spectral snow albedo obtained from the
18 reflectance measurements, together with the albedo modelled based on the SSK metric. The
19 overcast cases (23 December and 14 January) were both preceded by snowfall events, but the
20 albedo on 23 Dec was lower than on 14 Jan. The highest albedo during our measurement
21 campaign was observed on 26 December, in correspondence with the finest surface snow
22 generated by a snowdrift event. Our successive albedo spectra until 6 January revealed a
23 progressive albedo decrease associated with the snow ageing. On 12 January, albedo slightly
24 increased for $\lambda < 1.4 \mu\text{m}$, as a result of a change in the composition of the snow crystal
25 population at the surface: in addition to the rounded polycrystals typical of 5 and 6 January,
26 also faceted surface hoar was present (See Sect. 2.3). In the last two case studies (14 and 19
27 January) albedo was higher than on 5 and 6 January at almost all wavelengths, as a
28 consequence of the light snowfall during the previous days.

29 Mean differences between modelled and observed albedo values are shown in Fig. 10. For
30 droxtals, the modelled albedo is in a good agreement with the observed albedo values for
31 $\lambda > 1.4 \mu\text{m}$ (Fig. 10b). The biases are small, and considering the impact of sampling and image

1 processing uncertainty, the computed values agree with the observations in all case studies in
2 Fig. 9. For shorter SWIR wavelengths, the modelled albedo applying droxtal shapes fits best
3 the observation-based albedo on 23 and 26 December, but generally overestimates it,
4 especially on 5 and 6 January (Fig. 9). Only on 14 January the modelled albedo tends to
5 underestimate the observations at all wavelengths. Spherical shapes underestimate the albedo
6 for $\lambda > 1.4 \mu\text{m}$ but produce a better match with the measurement-derived albedo than droxtal
7 shapes for $\lambda < 1.4 \mu\text{m}$, although both have a positive bias in this wavelength range (Fig. 10).
8 The reason for these case and wavelength-dependent differences between modelled and
9 measured albedo is addressed in Sect. 5.3.

10 **4.2 Surface broadband albedo and net shortwave radiation**

11 To examine the impact of the bias in the modelled albedo (Fig. 10) on the surface net
12 shortwave radiation, we calculated the broadband surface albedo (α_b) and broadband net
13 shortwave radiation (S_{wn}) in the whole solar spectrum (0.35-2.5 μm) and in three distinct
14 bands: 1.0-1.4 μm (where we got the largest albedo biases), 1.4-2.5 μm (where we got the
15 smallest albedo biases), and the whole interval 1.0-2.5 μm used in spectral albedo analysis.
16 The broadband downward irradiance was computed from the measurements of spectral
17 downward irradiance (Sect. 2.6), while the upward irradiance was derived by multiplying the
18 downward irradiance by the albedo computed using droxtals (for $\lambda = 0.35\text{-}2.5 \mu\text{m}$) and spheres
19 (for $\lambda = 1.0\text{-}2.5 \mu\text{m}$) and by the spectral albedo obtained from reflectance measurements (for
20 $\lambda = 1.0\text{-}2.5 \mu\text{m}$). The measurement- and model-derived broadband values are compared in
21 Table 54 for the three wavebands mentioned above, while the droxtal-modeled broadband
22 values encompassing the solar spectrum (0.35-2.5 μm) are used here only for evaluating the
23 fractional contributions of each waveband.

24 First, we note that the spectral partitioning of solar energy absorbed by snow differs greatly
25 from that of the incoming irradiance. On average, in the clear-sky (overcast) cases 80% (66%)
26 of the net shortwave radiation absorbed by the snow belonged to the 1.0-2.5 μm waveband,
27 which contributed 23% (14%) of the incoming irradiance, and 50% (28%) of the net
28 shortwave radiation belonged to the 1.4-2.5 μm waveband, which contributed only 9% (3%)
29 of the incoming irradiance. The disproportionally large contribution of the SWIR bands to the
30 net radiation results, of course, from the snow albedo being much lower than in the VNIR
31 region. Furthermore, in the clear-sky cases, the 1.4-2.5 μm region made the largest

1 contribution to the absorbed shortwave energy (50%), while in the overcast cases the largest
 2 contribution (roughly 38%) came from the 1.0-1.4 μm region. This occurs because clouds
 3 selectively absorb the shortwave radiation at the longest wavelengths and therefore shift the
 4 spectral distribution of irradiance toward the visible region.

5 Table 54 lists the mean surface albedo ($\overline{\alpha_{b,\Delta\lambda}}$) and net shortwave radiation ($\overline{Sw_{n,\Delta\lambda}}$, Wm^{-2})
 6 integrated over three distinct wavebands (1.0-1.4 μm , 1.4-2.5 μm , and 1.0-2.5 μm) during
 7 overcast and clear-sky conditions, together with the biases between model- and reflectance-
 8 based averages. As expected, the modelled $\overline{\alpha_{b,1.0-1.4}}$ using droxtals showed the largest
 9 positive albedo bias in the clear-sky cases. As the bias in $\overline{\alpha_{b,1.4-2.5}}$ was minimal, the bias of
 10 0.09 in $\overline{\alpha_{b,1.0-2.5}}$ was almost totally due to the bias in $\overline{\alpha_{b,1.0-1.4}}$. This positive albedo bias
 11 produced a negative bias of -15 Wm^{-2} in $\overline{Sw_{n,1.0-2.5}}$. However, it should be kept in mind that
 12 in the computation of the broadband albedo α_b , $\overline{\alpha_{b,1.0-2.5}}$ is weighted by the corresponding
 13 fraction of incoming irradiance, which is only 23%. Since in the visible region the albedo
 14 sensitivity to snow particle size is small, we presume that the bias in the modelled α_b is much
 15 more modest than in the 1.0-2.5 μm region. In overcast conditions, the mean bias in the
 16 droxtal based $\overline{\alpha_{b,1.0-2.5}}$ was minimal, and, consequently, the corresponding bias in
 17 $\overline{Sw_{n,1.0-2.5}}$ was negligible. Overall, spherical particles caused smaller $\overline{\alpha_{b,\Delta\lambda}}$ biases than
 18 droxtal particles in the clear-sky cases, because of the smaller positive bias in the 1.0-1.4 μm
 19 region. The biases in the sphere-based $\overline{\alpha_{b,\Delta\lambda}}$ and in the associated $\overline{Sw_{n,\Delta\lambda}}$ are in qualitative
 20 agreement with the biases obtained by Carmagnola et al. (2013) using the same modelling
 21 approach, although Carmagnola et al. showed the albedo and the absorbed energy integrated
 22 over different wavebands and therefore a direct quantitative comparison is not possible.

23 4.3 Comparison between measured r_{eff} and optically equivalent r_{oeff}

24 Figure 11 shows r_{eff} at the surface ($r_{eff,sur}$, red circles) and at 5 cm depth ($r_{eff,5cm}$, green
 25 circles), calculated according to Eq. (2). The $r_{eff,sur}$ increased from 26 December to 6
 26 January, and then it remained almost constant. Its range of variability was from 0.07 ± 0.01
 27 mm to 0.2 ± 0.1 mm. The mean relative (i.e., fractional) 5% and 95% subjectivity
 28 (representativeness) errors of $r_{eff,sur}$ (defined in Sect. 3.1.4) were $\pm 11\%$ (-15% and $+10\%$).
 29 The values of $r_{eff,5cm}$ were mostly lower than those of $r_{eff,sur}$, with best estimates between
 30 0.08 and 0.14 mm, but attained a high value of 0.3 ± 0.2 mm on 19 January. The effective
 31 variance v_{eff} , calculated according to Eq. (3), was larger at the surface than at 5 cm depth (not

1 shown), as expected considering the various mechanisms of crystal formation, fragmentation,
2 aggregation, and metamorphism occurring at the surface. v_{eff} at the surface tended to increase
3 from roughly 0.2 in the beginning of the period to 0.5 near its end, probably as a result of the
4 enhanced snow metamorphism during melting and under the large temperature gradients
5 caused by the diurnal cycle of insolation.

6 The optical effective radius r_{oeff} , defined as the effective radius corresponding to the spectral
7 albedo obtained from surface reflectance measurements, was determined by applying
8 DISORT iteratively for each case and wavelength. A lognormal size distribution was
9 assumed, with the effective variance of the SSK metric in the surface layer.

10 For each case study, we obtained r_{oeff} as a function of wavelength separately for spherical and
11 droxtal shapes. We averaged r_{oeff} in four wavebands, each 0.1 μm -wide, where the variation of
12 r_{oeff} was modest (intra-band standard deviations generally at most 4%) and the signal-to-noise-
13 ratio of the measured nadir reflectance was relatively high. The four wavebands were centred
14 at 1.05, 1.28, 1.70, and 2.20 μm .

15 In Fig. 11 the r_{oeff} at the four wavebands is compared to $r_{eff,sur}$ and $r_{eff,5cm}$. The striking
16 features of Fig. 11 are 1) a good agreement of optical and measured effective radius on 23 and
17 26 December and on 14 January, especially for droxtal shapes, and 2) the much larger r_{oeff} at
18 the shortest SWIR wavelengths (1.05 and 1.28 μm) compared to r_{SSK} and to r_{oeff} at the longest
19 SWIR wavelengths (1.70 and 2.20 μm) on the other days. In all the eight case studies, the
20 measured $r_{SSK,sur}$ and $r_{SSK,5cm}$ agreed rather well with r_{oeff} at the longest SWIR wavelengths
21 (1.70 and 2.20 μm), especially for droxtal shapes. Due to the smaller asymmetry parameter of
22 droxtals, larger droxtal particles than spherical particles are needed to produce the same snow
23 spectral albedo. Table 65 summarizes the mean r_{oeff} ($\overline{r_{oeff}}$) for the four considered
24 wavebands: in case of the droxtal shape, r_{oeff} at 1.05 and 1.28 μm was, respectively, almost
25 triple and double that at 1.70 and 2.20 μm . Comparing the $\overline{r_{oeff}}$ using droxtals with the mean
26 measured $\overline{r_{eff,sur}}$ (0.17mm, with 5% and 95% errors of -0.04 and +0.03 mm, respectively),
27 we see excellent agreement at $\lambda=1.70$ and 2.20 μm (with biases of -0.01 and +0.01 mm,
28 respectively) but strong overestimation at $\lambda=1.05$ and 1.28 μm (with biases of +0.26 and
29 +0.15 mm, respectively), consistent with the large positive bias in the simulated albedo (Fig.
30 10b). Indeed, if the model overestimates the albedo for the measured particle size, it will
31 require larger particles to obtain the observed albedo. The reason for the excessive simulated

1 snow albedo at the shortest SWIR, and the consequent overestimated r_{oeff} , will be discussed in
2 Sect. 5.3.

3 The errors in r_{oeff} represented with bars in Fig. 11 were propagated from the errors in the
4 modelled albedo ($E05_{\alpha, \text{mod}}$ and $E95_{\alpha, \text{mod}}$, described in Appendix [AB3](#)) and were
5 significantly larger at the shortest SWIR wavelengths (1.05 and 1.28 μm) than at the longest
6 SWIR wavelengths (1.70 and 2.20 μm). This arises from the fact that the albedo is much less
7 sensitive to r_{oeff} at the shortest SWIR wavelengths than at the longest SWIR wavelengths.

8 **4.4 Sensitivity of r_{oeff} to ρ_{snow} and v_{eff}**

9 The uncertainty in snow density is not expected to have a significant impact on the modelled
10 albedo and r_{oeff} (Carmagnola et al., 2013). We tested the albedo sensitivity to ρ_{snow} by
11 reducing and increasing the observed values by 20%. The root mean square difference from
12 the albedo obtained using the observed ρ_{snow} was at most 0.2% (0.4%) at $\lambda=1.1 \mu\text{m}$ for droxtal
13 (spherical) shapes.

14 We also studied the sensitivity of r_{oeff} to v_{eff} by comparing r_{oeff} obtained using v_{eff} equal to 0.1
15 and 0.6, which correspond to the extreme values of v_{eff} observed during the measurement
16 period. Overall, the impact of v_{eff} on r_{oeff} was negligible or modest, though increasing with
17 increasing r_{oeff} and wavelength. For $\lambda < 1.4 \mu\text{m}$, the difference in r_{oeff} between $v_{\text{eff}}=0.1$ and
18 $v_{\text{eff}}=0.6$ was minimal (less 4%), while in the wavebands centred at 1.7 and 2.2 μm the
19 difference reached a maximum of 13% and 18% for droxtals and spheres, respectively, thus
20 being of the same magnitude as the uncertainty in r_{oeff} associated to errors in the
21 measurement-derived spectral albedo. These results hold only for the range of r_{oeff} examined
22 here and cannot necessarily be extended to (e.g.) cases with very large snow particles.

23

24 **5 Discussion**

25 **5.1 Method applied to estimate the snow particle metric**

26 The traditional snow particle sampling procedure adopted here involves the destruction of the
27 3D matrix of the aggregated crystals and the breaking of the bonds between the crystals. Any
28 notion on the crystal orientation is lost. Therefore, in our analyses we assume that the crystals
29 do not have a preferred orientation, although in the case of snow surfaces exposed to

1 persistent and directionally constant strong winds this assumption would not necessarily hold.
2 Moreover, crystal growth driven by a strong temperature gradient is vertically oriented
3 (Schneebeli and Sokratov, 2004). The fragments of ice bonds present in our samples are
4 analysed in the same way as the snow particles, thus their contribution to the scattered and
5 absorbed radiation is accounted for.

6 The image processing protocol utilized in this study is very time consuming, but it is robust,
7 as it is adaptable to various degrees of image sharpness and contrast, and it guarantees a
8 reasonable degree of objectivity. Faster, more sophisticated and automatic methods to detect,
9 classify, and measure the snow crystals from 2D images can certainly be developed, also
10 utilizing the expertise matured in other fields (e.g., Lindqvist et al., 2012; Rizk et al., 2014).
11 The reliability and repeatability of the 2D image processing procedure is closely related to the
12 resolution of the camera's apparatus. The smallest snow particles need to include a minimum
13 number of pixels to allow calculations of the particle metric, as the effectiveness of spatial
14 moments has been shown to deteriorate when the object is less than about 15 pixels wide or
15 when parts of the objects are relatively small (Coakley and Doom, 1995). With a suitable
16 macro-objective and extension tubes, the picture resolution of present-day cameras becomes
17 much higher than the minimum size of snow crystal fragments. However, in the present
18 dataset, the low contrast between the snow particles and the background field required a pixel
19 averaging that reduced the image resolution, resulting in a final resolution comparable to the
20 minimum crystal dimension. To prevent this problem, the measurement setting should
21 provide a uniform illumination to the snow sample.

22 The adopted *SSK* metric is not affected by the extension of the crystal clusters possibly
23 present, as it is based on the tiniest protrusion of the detected objects. The distance
24 transformation method, applied to obtain the particle skeleton from which the *SSK* metric is
25 calculated, has also previously been used to derive particle metrics from image processing
26 (Fily et al., 1997; Gay et al., 2002; Hildebrand and Rügsegger, 1997; Schneebeli and
27 Sokratov, 2004). Our results (Figs. 9-11) show that, in several cases, the r_{eff} obtained from the
28 measured *SSK* metric distributions matches quite well the sphere-based r_{oeff} and even better
29 the droxtal-based r_{oeff} . ~~Thus, we can conclude~~ This supports the hypothesis that our method is
30 suitable to measure the particle dimension that best corresponds to its scattering properties.

31 Computational and digital technology is continuously developing, facilitating the image
32 processing procedure. However, sizing snow particles through image processing will always

1 remain a time consuming technique compared to indirect optical methods (Arnaud et al.,
2 2011, Berisford et al., 2013; Gallet et al., 2009; Painter et al., 2007). The suitability of a
3 method should be evaluated on the basis of time limitations and availability of technical
4 equipment, and above all depending on the research applications.

5 **5.2 Impact of particle shape on albedo and $r_{o\text{eff}}$ simulations**

6 The albedo modelled utilizing observed r_{eff} , and the $r_{o\text{eff}}$ modelled on the basis of observed
7 reflectance depend on the applied particle shape (Figs. 9-11 and Table 65). The differences
8 between the modelling results applying spheres and droxtals are most distinct at the shortest
9 SWIR, with the droxtal-based albedo being ~10% larger than the sphere-based albedo at
10 $\lambda < 1.4 \mu\text{m}$ (Fig. 10), and the droxtal-based $r_{o\text{eff}}$ being on average 60% (40%) larger than the
11 sphere-based $r_{o\text{eff}}$ at $\lambda < 1.4 \mu\text{m}$ ($\lambda > 1.4 \mu\text{m}$) (Table 65). These results are close to those obtained
12 by Kokhanovsky and Zege (2004) using fractal shape. The comparison between modelled and
13 observed albedo at $\lambda > 1.4 \mu\text{m}$ (Figs. 9 and 10) confirmed our expectations, i.e. that the droxtal
14 shape better represents the optical properties of the snow particles compared to spheres, when
15 SSK is used as r_{eff} in the albedo modeling. This is in agreement with previous results: over the
16 Antarctic plateau, the particle shape assumption of aggregate of columns provided a much
17 better agreement with measured radiances than the equivalent sphere-based assumption (Jin et
18 al., 2008). Moreover, a large variety of observations and model calculations demonstrated that
19 spherical particles propagate light deeper than real snow (Libois et al., 2013). In general,
20 spherical particles can cause a large underestimation of the visible reflectance compared to
21 more faceted and realistic particle shapes (Neshyba et al., 2003; Grenfell et al., 2005;
22 Kokhanovsky and Zege, 2004; Picard et al., 2009, Tedesco and Kokhanovsky, 2007). Picard
23 et al. (2009) concluded that the $r_{o\text{eff}}$ estimated from albedo measurements with an unknown
24 particle shape has a $\pm 20\%$ error. Indeed, an equally good fit with observed albedo can be
25 obtained by modelling snow particles with different snow particle shapes, provided that the
26 particle size (and its vertical profile) is a fitting parameter (Kokhanovsky and Zege, 2004; Jin
27 et al., 2008).

28 Some previous studies have shown a good fit between sphere-based albedo and observations
29 at several wavelengths, when the utilized r_{eff} was the measured shortest particle dimension
30 (Aoki et al., 2000, 2003), or the r_{VA} was obtained from stereological measurements (Painter
31 and Dozier, 2004) or from SSA measurements (Carmagnola et al., 2013). We suspect that the

1 match with observations when r_{VA} was applied was due to the compensation of two errors: an
2 albedo underestimation caused by the spherical approximation, and an albedo overestimation
3 caused by the use of r_{VA} , which in the case of irregular and concave snow particles is smaller
4 than r_{VP} . However, our results also show that in some cases, under direct illumination, the
5 spherical shape assumption may give comparable or better results than the droxtal shape
6 assumption (Fig. ~~913 (c) and (d)~~). The reason behind this finding is discussed in detail in the
7 next section.

8 **5.3 Model discrepancies**

9 We obtained a remarkably good match between the albedo obtained from observations and
10 the albedo modelled applying droxtal shapes and the observed *SSK* metric at $\lambda > 1.4 \mu\text{m}$. On
11 the contrary, at $\lambda < 1.4 \mu\text{m}$ snow albedo was largely overestimated in most cases, in particular
12 using droxtals. Consequently, at $\lambda < 1.4 \mu\text{m}$ the r_{oeff} calculated from the observation-derived
13 albedo was much larger than at longer wavelengths. In only one case (on 14 January) albedo
14 was underestimated at all wavelengths, most probably because the fresh snow still present at
15 the time of the nadir-reflectance measurements had already undergone a strong
16 metamorphism 1.5 hours later, when the snow particles were photographed (see Table 1), due
17 to the intense melting that took place on that day (Fig. ~~21~~).

18 The discrepancy between modelled and observed albedo at some wavebands when at the same
19 time a good match is obtained at other wavebands has been frequently reported (Aoki et al.,
20 2000, 2007; Carmagnola et al., 2013; Domine et al., 2006; Fily et al., 1997; Grenfell et al.,
21 1994; Kuchiki et al., 2009). Equivalently, this translates into a change of r_{oeff} with changing
22 wavelengths.

23 The use of r_{VA} (or *SSA*) as r_{eff} has often resulted in a rather good simulation (or slight
24 overestimation) of the visible albedo, and in a significant underestimation of the albedo at
25 $\lambda > 1.4 \mu\text{m}$ (Grenfell et al., 1994; Painter and Dozier, 2004; Carmagnola et al., 2013). When
26 half the shortest particle dimension was used as r_{eff} , a similar result was obtained in some
27 cases (Aoki et al, 2007; Kuchiki et al., 2009), while in another case a good match between
28 modelled and observed albedo was achieved at $\lambda > 1.4 \mu\text{m}$, while albedo was overestimated at
29 $1.0 < \lambda < 1.4 \mu\text{m}$ (Aoki et al., 2000). This last case is in agreement with our findings (Fig. 10),
30 and in line with Kokhanovsky et al. (2011), who retrieved r_{oeff} much larger at $\lambda = 0.865 \mu\text{m}$
31 than at $\lambda = 1.24 \mu\text{m}$. In all these studies, the bias between simulated and observed albedo was

1 more or less positive at $\lambda < 1.4 \mu\text{m}$ and more or less negative at $\lambda > 1.4 \mu\text{m}$. Similarly, the
2 reported r_{oeff} calculated from reflectance measurements were much smaller at $\lambda > 1.4 \mu\text{m}$ than
3 at $\lambda < 1.4 \mu\text{m}$ (Aoki et al., 2007; Fily et al., 1997; Kuchiki et al., 2009).

4 Traditionally, these results are explained with the particle size differences in the vertical
5 profile of the snowpack: the albedo at shorter wavelengths conveys snow particle size
6 information from deeper layers than the albedo at longer wavelengths. At $\lambda > 1.4 \mu\text{m}$ the
7 penetration depth of light is only a few millimetres (Fig. 8), and often this thin, uppermost
8 snow layer is characterized by smaller particles than the deeper layers (Aoki et al., 2000;
9 Carmagnola et al., 2013). An ad hoc vertical profile of snow particle size in the uppermost
10 few millimetres of the snowpack has sometimes been utilized to conciliate modelled and
11 observed albedo (Grenfell et al., 1994). However, when applying a detailed vertical profile of
12 particle size in the albedo calculations, the discrepancies with observations were not solved
13 (Aoki et al., 2000, 2007; Carmagnola et al., 2013). Moreover, in our case, snow particles were
14 larger at the surface than at deeper layers (Fig. 11), as a result of the intense snow
15 metamorphism occurring around midday with direct insolation, positive sensible heat flux,
16 and temperature close to the melt point.

17 Some other hypotheses have been formulated to explain the underestimation of the modelled
18 albedo at $\lambda > 1.4 \mu\text{m}$: Carmagnola et al. (2013) attributed it to the uncertainty on the value of
19 the ice refractive index, whereas Aoki et al. (2007) to the fine structure of the thin sun crust
20 present at the surface. This last hypothesis, however, was not confirmed by later observations,
21 when wet, melting snow without sun crust still gave rise to the same discrepancy (Kuchiki et
22 al., 2009). Kuchiki et al. explained the underestimation of the satellite retrieved r_{oeff} compared
23 to observations in relation to the microstructure of the snow surface. They hypothesized that
24 the small irregularities and protrusions present on the surface of large particles had a
25 dominant contribution to the reflected light at the longest SWIR.

26 On the basis of our results, do not support the hypothesis that the model discrepancies are
27 primarily related to the uncertainty on the value of the ice refractive index, as the wavelength
28 dependence of our modelled albedo biases was case dependent. we cannot exclude the
29 possibility that uncertainties in ice refractive index may contribute to the wavelength
30 dependence of r_{oeff} . If this were the main reason for the wavelength dependence, we would
31 expect that the relative difference in r_{oeff} between different wavelengths is similar from case to
32 case. Indeed, we note from Fig. 11 that the best estimate of r_{oeff} at $\lambda = 2.20 \mu\text{m}$ is consistently

1 slightly larger than that at $\lambda=1.70 \mu\text{m}$ (in relative terms, by 13-20% depending on case).
2 However, the difference in r_{oeff} between the weakly absorbing wavelengths ($\lambda=1.05 \mu\text{m}$ and
3 $\lambda=1.28 \mu\text{m}$) and $\lambda=1.70 \mu\text{m}$ depends strongly on the case: the relative difference between
4 $1.05 \mu\text{m}$ and $1.70 \mu\text{m}$ varies from 45 to 391%, and that between $\lambda=1.28 \mu\text{m}$ and $\lambda=1.70 \mu\text{m}$
5 from 53% to 158%. This strong case dependency suggests that uncertainties in refractive
6 index are probably not the primary contributing factor to the wavelength dependence of r_{oeff} .

7 Instead, the explanation given by Kuchiki et al. (2009) better suits our findings. Indeed, their
8 surface conditions strongly resemble our observations. We obtained an almost wavelength
9 independent r_{oeff} when the surface was rather smooth and homogeneous because of fresh snow
10 (on 23 December and 14 January) and drifted snow (on 26 December). The difference in
11 optical effective particle radius between different wavelengths was largest on 5 and 6 January,
12 when strong melting occurred and large, irregular surface snow particles with thin protrusions
13 coexisted with smaller particles (see Table 3), causing a rough texture in the millimetre scale.
14 This seems a rather common feature of the Antarctic snow surface, also observed on the high
15 plateau (Gallet et al., 2014). At the shortest SWIR wavelengths, photons can penetrate several
16 millimetres into the snowpack (see Fig. 7), and their absorption/scattering takes place with
17 higher probability in the biggest snow particles, where the optical path is longest. Thus, the
18 relative contribution of the biggest particles to the reflected irradiance is larger than the
19 contribution of their thin branches. On the other hand, at the longest SWIR wavelengths
20 photons have very short optical path in the snow (the penetration depth is smaller than 1 mm),
21 and therefore, they have low chances to penetrate beyond the tiniest protruding branches,
22 which then contribute to the reflected irradiance in much larger proportion than at the shortest
23 SWIR wavelengths. This may explain why we obtained consistent agreement between r_{eff}
24 and r_{oeff} at the longest SWIR wavelengths in all case studies, when assuming droxtal-shaped
25 snow particles.

26 We clearly observed a relationship between the modelling biases at the shortest SWIR and the
27 mm-scale surface roughness. Roughness increased during snowmelt as compared to
28 immediately after snowfall, as previously observed (Anttila et al., 2014; Fassnacht et al.,
29 2009). The cavities developed during the melting trap a fraction of the reflected light into
30 their walls, particularly at the shortest wavelengths due to multiple reflections between the
31 walls. Thus, at those shortest wavelengths the albedo is lower for a rough surface (in the
32 millimetre scale) than for a flat surface, and r_{oeff} is larger than r_{eff} . The modelling biases may

1 have also been affected by the larger (cm-scale) surface roughness such as sastrugi, and their
2 orientation with respect to the solar position. Indeed, the presence of sastrugi causes an albedo
3 reduction with respect to a flat snow surface (Kuhn, 1974), and this effect depends on the
4 albedo itself, being stronger for intermediate values of albedo (i.e., in the near-infrared
5 spectral range, Warren et al., 1998). On 26 December, when r_{eff} was almost identical for all
6 wavelengths, surface striations were small, and the solar zenith angle at the time of the
7 spectral reflectance measurements was smaller than in the following days. On 5 and 6
8 January, when r_{eff} for the shortest SWIR was largest, the snow metamorphism due to the
9 melting was very strong and caused a deepening of the sastrugi. Later, the melting continued,
10 but the occasional snowfall events reduced the surface roughness at the cm-scale.

11 Following this interpretation, when the droxtal shape is applied, the *SSK* metric seems to
12 rather well represent the scattering properties of the snow at $\lambda > 1.0 \mu\text{m}$ when the surface is
13 smooth and the snow particle population is homogeneous in size, but it overestimate r_{eff} for
14 $1.0 < \lambda < 1.4 \mu\text{m}$ when there is a 10-20 times size difference among the coexisting snow
15 particles and branches, and the millimetre- and centimetre-scale surface roughness is
16 significant. These findings strongly suggest that a single particle metric distribution is not
17 sufficient to describe the scattering properties of surfaces composed of mixed-size particles.
18 This may have profound implications in the interpretations of satellite-based reflectance
19 measurements, presently based on single size distributions and on models that neglect the
20 surface roughness (Painter et al., 2003; Lyapustin et al., 2009). Thus, our results highlight a
21 relevant observational and modelling gap. Until now, studies on the impact of surface
22 roughness on snow albedo have focused mainly on the effect of sastrugi (Leroux and Fily,
23 1998; Warren et al., 1998; Hudson and Warren, 2007; Lyapustin et al., 2010; Zhuravleva and
24 Kokhanovsky, 2011). Warren (1982) indicates that surface roughness features reduce the
25 albedo when their dimension is comparable to or larger than the penetration depth of light.
26 This implies that surface roughness of amplitude $\gtrsim 10 \text{ cm}$ (such as sastrugi) reduces the
27 visible albedo, but much smaller irregularities can affect the near-infrared albedo.
28 Nevertheless, only few measurements of millimetre-scale snow surface roughness have been
29 carried out so far (Anttila et al., 2014; Frassnacht et al., 2009; Manninen, 1997), and they
30 have not yet been applied to interpret the surface albedo.

31

1 6 Conclusions

2 This study illustrates a method to extract a snow particle size metric, the *SSK* (shortest
3 skeleton branch), from 2D snow macrophotos. From the metric distributions, we calculated
4 the effective particle size r_{eff} , which was then used to model the surface albedo. The *SSK*
5 metric provided albedo values that agreed well with the observed albedo values for $\lambda > 1.4 \mu\text{m}$,
6 especially when the snow particles were modelled with droxtal shapes (Fig. 9). For $\lambda < 1.4 \mu\text{m}$,
7 a good fit between the modelled and the observed albedo was still present in some cases, but,
8 on average, a large positive bias was observed (Fig. 10).

9 The measured r_{eff} were then compared to the optical effective radius r_{oeff} calculated from the
10 surface spectral albedo assuming that snow is optically equivalent to a collection of spheres or
11 droxtals, which have the same r_{VP} as the snow particles. Considering the cases when the
12 surface was rather smooth and homogeneous because of fresh snow (on 23 December and 14
13 January) and drifted snow (on 26 December), we found that r_{eff} corresponded to r_{oeff}
14 remarkably well at all wavelengths, particularly for droxtal shape calculations (Fig. 11). We
15 explain this finding by arguing that the r_{eff} based on the *SSK* metric is a close approximation
16 of the r_{VP} of the snow particles. In the other cases, the optical effective radius r_{oeff} depended
17 on wavelength, confirming previous studies (Aoki et al., 2000, 2007; Carmagnola et al., 2013;
18 Domine et al., 2006; Fily et al., 1997; Grenfell et al., 1994; Kuchiki et al., 2009), and r_{eff}
19 corresponded to r_{oeff} only at the longest SWIR wavelengths. Our observations revealed that
20 the wavelength dependence of r_{oeff} varied with the seasonal evolution of the snow surface
21 layer. We interpreted these findings on the basis of the observed shape and size distributions
22 of the snow particles at the surface, and based on the evolution of the millimetre- and
23 centimetre-scale surface roughness features. We suggest that when large, irregular particles
24 such as surface hoar and faceted polycrystals were present at the surface, the contribution of
25 the largest particles to the reflected irradiance dominated at the shortest SWIR wavelengths,
26 while the contribution of the thinnest protrusions of the irregular crystals dominated at the
27 longest SWIR wavelengths. This type of particle population developed during the alternation
28 of nocturnal freezing and diurnal melting and was associated with mm-scale surface cavities,
29 which possibly contributes to reduce the albedo at the shortest SWIR wavelengths. These
30 results indicate that more than just one particle metric distribution is needed to characterize
31 the snow scattering properties at all optical wavelengths, and underline the limitation of the

1 plane parallel assumption made in many snow radiative transfer models (Lyapustin et al.,
2 2009; Painter et al, 2003).

3 Considering all uncertainties in the observations, in the methods of analysis, and in the
4 modelling assumptions, the very good agreement between r_{oeff} and r_{eff} and between modelled
5 and observed albedo in the cases of smooth and homogeneous surfaces is encouraging. It
6 suggests that the method applied to measure snow particle size is adequate for optical
7 applications, that the *SSK* metric offers a good synthesis of the particle's physical dimension
8 relevant for light scattering, and that the droxtal shape represents the scattering properties of
9 the snow particles better than the spherical shape. In the cases of rougher surfaces with
10 heterogeneous particle population, the *SSK* metric characterizes the scattering by snow only
11 for $\lambda > 1.4 \mu\text{m}$. For shorter wavelengths, a larger metric should be applied, and this will be
12 investigated in our future studies.

13 The analysed wavelength range (1.0-2.5 μm) is critical from the point of view of the surface
14 radiation budget, as it included 80% (66%) of the net shortwave radiation absorbed by the
15 snow during the clear-sky (overcast) cases examined. In the overcast cases, all characterized
16 by fresh snow at the surface, the negligible bias of the droxtal-based modeled albedo in the
17 1.0-2.5 μm range resulted in a negligible bias in the absorbed shortwave radiation. In the
18 clear-sky cases, the positive bias of the droxtal-based modelled albedo caused an average
19 underestimation of the absorbed shortwave radiation of about -15 Wm^{-2} .

20 The impact of millimetre-scale snow surface roughness on the surface albedo needs to be
21 better understood. A field campaign addressing the characterization of snow roughness
22 texture with the dimension ranging from centimetres to millimetres is being planned, with the
23 goal of measuring the roughness both in the limited field-of-view of ground-based spectral
24 albedo sensors and in the large footprint area of remote sensing sensors.

25

26 **Appendix A: Calculation of errors in albedo, r_{eff} , and v_{eff}**

27 Throughout this paper, uncertainty in albedo, r_{eff} , and v_{eff} is estimated in terms of the “5%
28 and 95% errors” (E05 and E95, respectively). The 5% (95%) error is defined as the difference
29 between the lower (upper) limit of the 90% confidence interval and the best estimate.

30 **A1: Errors in the albedo derived from reflectance measurements**

1 We briefly summarize here the independent errors in the measurement-derived albedo:

- 2 1) Error in repeatability of the snow reflectance σ_{rpt} , equal to the normalized standard
3 deviation of reflectance among 30 consecutive spectra;
- 4 2) Error in horizontal leveling of the reference spectralon σ_{ref} , equal to the normalized
5 standard deviation of spectralon reflectance among 30 consecutive spectra;
- 6 3) Bias due to the tilting of the snow surface, positive in the downhill direction
7 ($\Delta_{tilt,down}$) and negative in the uphill direction ($\Delta_{tilt,up}$);
- 8 4) 5% and 95% errors of Φ ($E05_{\Phi}$ and $E95_{\Phi}$, respectively), which propagate to the
9 hemispherical albedo when applying Eq. B4 (see Appendix B).

10 The resulting 5% and 95% errors in the measurement-derived albedo ($E05_{\alpha,obs}$ and $E95_{\alpha,obs}$,
11 respectively) are:

$$12 \quad E95_{\alpha,obs} = \sqrt{c^2 \cdot (\sigma_{rpt}^2 + \sigma_{ref}^2) + \Delta_{tilt,down}^2 + E95_{\Phi}^2} \quad (A1)$$

$$13 \quad E05_{\alpha,obs} = -\sqrt{c^2 \cdot (\sigma_{rpt}^2 + \sigma_{ref}^2) + \Delta_{tilt,up}^2 + E05_{\Phi}^2} \quad (A2)$$

14 where $c=1.6456$ is the factor that gives the 5% and 95% confidence limits of the two normally
15 distributed errors σ_{rpt} and σ_{ref} .

16 **A2: Errors in r_{eff} and v_{eff}**

17 The independent errors in the particle metric distributions (described in Section 3.1.4) that
18 propagate to the calculation of r_{eff} and v_{eff} are:

- 19 1) 5% and 95% subjectivity errors of the SSK metric distributions ($E05_{sub}$ and $E95_{sub}$,
20 respectively). They are calculated as the averaged root-mean-square error between the
21 SSK metric obtained by one experienced and two unexperienced persons in image
22 processing, divided by the square root of the number of cases, and multiplied by the
23 coefficient $c=1.6456$.
- 24 2) 5% and 95% representativeness errors of the SSK metric distributions ($E05_{rpr}$ and
25 $E95_{rpr}$, respectively). Depending on whether the error in r_{eff} or v_{eff} was considered, the
26 bootstrap realizations were arranged according to their r_{eff} or v_{eff} .

The resulting 5% and 95% errors in r_{eff} and v_{eff} ($E05_{r_{eff},v_{eff}}$ and $E95_{r_{eff},v_{eff}}$ respectively) are:

$$E95_{r_{eff},v_{eff}} = \sqrt{E95_{sub}^2 + E95_{rpr}^2} \quad (A3)$$

$$E05_{r_{eff},v_{eff}} = -\sqrt{E05_{sub}^2 + E05_{rpr}^2} \quad (A4)$$

When averaging over several cases, the error of the mean r_{eff} (v_{eff}) is obtained from the mean of the errors of all the cases divided by the square root of the number of cases (see Table 5).

A3. Errors in the difference between model- and measurement-derived albedo

The errors expressed by Eqs. (A3) and (A4) propagate to the model-derived albedo. As the smallest particles of the confidence interval generate the highest albedo, the 5% error of r_{eff} ($E05_{r_{eff},v_{eff}}$) corresponds to the 95% error of the model-derived albedo ($E95_{\alpha,mod}$). Vice versa, the largest particles generate the smallest albedo, therefore $E95_{r_{eff},v_{eff}}$ is proportional to the 5% error of the model-derived albedo ($E05_{\alpha,mod}$). The 5% and 95% errors of the bias between model- and measurement-derived albedo ($E05_{\Delta\alpha}$ and $E95_{\Delta\alpha}$, respectively) are calculated as:

$$E95_{\Delta\alpha} = \sqrt{E95_{\alpha,obs}^2 + E95_{\alpha,mod}^2} \quad (A5)$$

$$E05_{\Delta\alpha} = -\sqrt{E05_{\alpha,obs}^2 + E05_{\alpha,mod}^2} \quad (A6)$$

When averaging over several cases, the errors of the mean bias are obtained from the mean of the errors of all the cases divided by the square root of the number of cases (see Fig. 10).

Appendix BA: Calculation of hemispherical albedo using nadir reflectance and anisotropic reflectance factor measured by Hudson et al. (2006)

The measured snow nadir reflectance (I_n) was integrated over a FOV of 25°, and therefore it is expressed as:

$$I_n(\theta_0) = \frac{\int_0^{360^\circ} \int_0^{12.5^\circ} I_r(\theta_0, \theta_v, \phi) \cos\theta_v \sin\theta_v d\theta_v d\phi}{F_0}, \quad (BA1)$$

1 where I_r is the radiance reflected into a particular direction ($\text{W m}^{-2} \text{sr}^{-1} \mu\text{m}^{-1}$), θ_v is the viewing
 2 zenith angle, ϕ is the relative azimuth angle, and F_0 is the incident irradiance at that particular
 3 θ_0 ($\text{W m}^{-2} \mu\text{m}^{-1}$). Our objective is to obtain α , which reads as:

$$4 \quad \alpha(\theta_0) = \frac{\int_0^{360^\circ} \int_0^{90^\circ} I_r(\theta_0, \theta_v, \phi) \cos \theta_v \sin \theta_v d\theta_v d\phi}{F_0}. \quad (\text{BA2})$$

5 Due to the anisotropic scattering by the snow particles, the diffuse radiation reflected by the
 6 snow surface is not isotropic, but it is distributed according to the bidirectional reflectance
 7 distribution function (BRDF). In principle, knowing the snow BRDF it is possible to convert
 8 the radiances measured at a specific viewing angle to spectral albedo. Hudson et al. (2006)
 9 calculated the snow BRDF at Dome Concordia, over the Antarctic Plateau, in the form of
 10 anisotropic reflectance factor (Φ), defined as π times the ratio of radiance reflected into a
 11 particular direction, to the reflected flux:

$$12 \quad \Phi(\theta_0, \theta_v, \phi) = \frac{\pi I_r(\theta_0, \theta_v, \phi)}{\int_0^{360^\circ} \int_0^{90^\circ} I_r(\theta_0, \theta_v, \phi) \cos \theta_v \sin \theta_v d\theta_v d\phi}. \quad (\text{BA3})$$

13 By integrating Φ in the 25° FOV of the ASD spectroradiometer (Φ_n) and combining Eqs.
 14 ([BA1](#)), ([BA2](#)), and ([BA3](#)) we get:

$$15 \quad \alpha(\theta_0) = \frac{I_n(\theta_0)}{\Phi_n(\theta_0)}. \quad (\text{BA4})$$

16 We parameterized Φ_n based on the measurements of Hudson et al. (2006), who derived Φ
 17 from their observations of snow reflectance at various viewing zenith angles and relative
 18 azimuth angles, done using an ASD with a 15° FOV. Dome Concordia is characterized by
 19 very fine snow particles, which maximize the snow reflectance, and by small and randomly
 20 distributed sastrugi, which affect Φ especially at the large viewing zenith angles, and reduce
 21 the anisotropy of Φ compared to that of sunlight reflected from a flat snow surface (Hudson
 22 and Warren, 2007). We estimate that the surface roughness features at Aboa are quite similar
 23 to the ones present at Dome Concordia. In any case, the results by Hudson et al. (2006) have
 24 also been confirmed by measurements carried out in the Arctic (Lyapustin et al., 2010). We
 25 utilized the subset of Hudson et al.'s Φ data at $\theta_v = 7.5^\circ$ (available online as auxiliary Table
 26 [jgrd13053-sup-0003-ts02.txt](#)) to derive a specific parameterization of Φ_n as a function of their
 27 measured I_n (auxiliary Table [jgrd13053-sup-0002-ts01.txt](#)) and $\cos \theta_0$ using a multi-linear
 28 regression model:

$$\ln\Phi_n = a + b \cdot \ln I_n + c \cdot \cos(\theta_0), \quad \begin{cases} a = -0.25 \pm 0.03 \\ b = 0.173 \pm 0.002 \\ c = 0.40 \pm 0.05 \end{cases} \quad (\text{BA5})$$

The I_n was measured applying a similar procedure as that used in this study, with the input fiber optic of the ASD receiving light reflected from a Spectralon plate in a 15° FOV. The regression coefficients a , b , and c were determined with the least squares method and are given in Eq. (BA5) with the 90% confidence intervals. The square of the linear correlation coefficient is 0.938. Figure BA1 illustrates the data utilized for the derivation of Eq. (BA5) (black dots) and the fitted multi-linear model (red dots): it shows that Φ_n is smaller than 1 and it increases with increasing I_n . Indeed, Hudson et al. (2006) observed that snow is brightest ($\Phi > 1$) when viewed near the horizon and darkest ($\Phi < 1$) when viewed near nadir, and this anisotropy decreases with increasing I_n .

Particle size variations and changes in the orientations and dimensions of the surface roughness features during the progress of the season represent sources of uncertainty for the Φ parameterization. Indeed, an increase in particle size increases the anisotropy of the BRDF pattern, strengthening the forward reflectance peak of snow. Because of the short path length of SWIR light into the snow compared to the visible wavelengths, uncertainties are particularly significant in this waveband region. Sastrugi orientation did not change during our measurement period, but their dimension increased, possibly causing a decreased BRDF anisotropy. A further source of uncertainty is that the data for $\theta_v=7.5^\circ$ in Hudson et al. (2006) do not represent exactly the range of viewing angles needed for Φ_n (i.e., $\theta_v=0-12.5^\circ$). First, $\theta_v=7.5^\circ$ corresponds formally to $\theta_v=0-15^\circ$, and more importantly, Hudson et al. (2006) did not actually measure radiances at $\theta_v=7.5^\circ$ but rather used median values for $\theta_v=22.5^\circ$, which represents the range $\theta_v=15-30^\circ$. Without a better method to quantify these uncertainties on Φ_n , we estimated the confidence intervals for Φ_n utilizing the 90% confidence intervals of the regression coefficients in Eq. (BA5) ($E_{05\Phi}$ and $E_{95\Phi}$, respectively). We then utilized Eq. (BA4) to calculate the spectral albedo.

Hudson et al. (2006) assumed that their measured I_n in overcast conditions is equivalent to the diffuse α . However, in fact, even in a case with isotropic incident radiation, I_n tends to be smaller than α , especially at strongly absorbing wavelengths (i.e., low α) where first-order scattering makes a large contribution to the reflected radiance. The fundamental reason for this is the anisotropic scattering by snow particles. Reflectance towards the zenith requires

scattering in the backward hemisphere ($90^\circ - 180^\circ$), but forward scattering dominates in the case of snow particles. Therefore, we applied Eqs. (BA4) and (BA5) to all our cases, using an effective solar zenith angle ($\theta_{0,eff}$) of 55° for the I_n measured in overcast conditions. This is somewhat an ad-hoc choice, based on the notion that in two-stream approximations in which the angular distribution of diffuse radiation is not represented explicitly, it is typically approximated with a diffusivity factor of $D = 1.5-2$ (Edwards and Slingo, 1996), corresponding to $\theta_{0,eff} = \cos^{-1}(1/D) = 48.2^\circ - 60^\circ$. Varying $\theta_{0,eff}$ in this range in Eq. (B5) would change the resulting snow albedo at most by 3-4% compared to the results for $\theta_{0,eff} = 55^\circ$.

Appendix B: Calculation of errors in albedo, r_{eff} , and v_{eff}

Throughout this paper, uncertainty in albedo, r_{eff} , and v_{eff} is estimated in terms of the “5% and 95% errors” (E05 and E95, respectively). The 5% (95%) error is defined as the difference between the lower (upper) limit of the 90% confidence interval and the best estimate.

B1: Errors in the albedo derived from reflectance measurements

We briefly summarize here the independent errors in the measurement-derived albedo:

- 1) Error in repeatability of the snow reflectance σ_{rpt} , equal to the normalized standard deviation of reflectance among 30 consecutive spectra;
- 2) Error in horizontal leveling of the reference spectralon σ_{ref} , equal to the normalized standard deviation of spectralon reflectance among 30 consecutive spectra;
- 3) Bias due to the tilting of the snow surface, positive in the downhill direction ($\Delta_{tilt,down}$) and negative in the uphill direction ($\Delta_{tilt,up}$);
- 4) 5% and 95% errors of Φ ($E05_\Phi$ and $E95_\Phi$, respectively), which propagate to the hemispherical albedo when applying Eq. A4 (see Appendix A).

The resulting 5% and 95% errors in the measurement-derived albedo ($E05_{\alpha,obs}$ and $E95_{\alpha,obs}$, respectively) are:

$$E95_{\alpha,obs} = \sqrt{c^2 \cdot (\sigma_{rpt}^2 + \sigma_{ref}^2) + \Delta_{tilt,down}^2 + E95_\Phi^2} \quad (B1)$$

$$E05_{\alpha,obs} = -\sqrt{c^2 \cdot (\sigma_{r_{pt}}^2 + \sigma_{r_{eff}}^2) + \Delta_{lit,up}^2} + E05_{\Phi} \quad (B2)$$

where $c=1.6456$ is the factor that gives the 5% and 95% confidence limits of the two normally distributed errors $\sigma_{r_{pt}}$ and $\sigma_{r_{eff}}$.

B2: Errors in r_{eff} and v_{eff}

The independent errors in the particle metric distributions (described in Section 3.1.4) that propagate to the calculation of r_{eff} and v_{eff} are:

1) 5% and 95% subjectivity errors of the SSK metric distributions ($E05_{sub}$ and $E95_{sub}$, respectively). They are calculated as the averaged root-mean-square error between the SSK metric obtained by one experienced and two unexperienced persons in image processing, divided by the square root of the number of cases, and multiplied by the coefficient $c=1.6456$.

2) 5% and 95% representativeness errors of the SSK metric distributions ($E05_{ppr}$ and $E95_{ppr}$, respectively). Depending on whether the error in r_{eff} or v_{eff} was considered, the bootstrap realizations were arranged according to their r_{eff} or v_{eff} .

The resulting 5% and 95% errors in r_{eff} and v_{eff} ($E05_{r_{eff},v_{eff}}$ and $E95_{r_{eff},v_{eff}}$, respectively) are:

$$E95_{r_{eff},v_{eff}} = \sqrt{E95_{sub}^2 + E95_{ppr}^2} \quad (B3)$$

$$E05_{r_{eff},v_{eff}} = -\sqrt{E05_{sub}^2 + E05_{ppr}^2} \quad (B4)$$

When averaging over several cases, the error of the mean r_{eff} (v_{eff}) is obtained from the mean of the errors of all the cases divided by the square root of the number of cases (see Table 4).

B3. Errors in the difference between model and measurement-derived albedo

The errors expressed by Eqs. (B3) and (B4) propagate to the model-derived albedo. As the smallest particles of the confidence interval generate the highest albedo, the 5% error of r_{eff}

1 ~~($E_{05_{r_{eff},v_{eff}}}$) corresponds to the 95% error of the model derived albedo ($E_{95_{\alpha,mod}}$). Vice~~
 2 ~~versa, the largest particles generate the smallest albedo, therefore $E_{95_{r_{eff},v_{eff}}}$ is proportional~~
 3 ~~to the 5% error of the model derived albedo ($E_{05_{\alpha,mod}}$). The 5% and 95% errors of the bias~~
 4 ~~between model and measurement derived albedo ($E_{05_{\Delta\alpha}}$ and $E_{95_{\Delta\alpha}}$, respectively) are~~
 5 ~~calculated as:~~

$$6 \quad E_{95_{\Delta\alpha}} = \sqrt{E_{95_{\alpha,obs}}^2 + E_{95_{\alpha,mod}}^2} \quad (B5)$$

$$7 \quad E_{05_{\Delta\alpha}} = -\sqrt{E_{05_{\alpha,obs}}^2 + E_{05_{\alpha,mod}}^2} \quad (B6)$$

8 ~~When averaging over several cases, the errors of the mean bias are obtained from the mean of~~
 9 ~~the errors of all the cases divided by the square root of the number of cases (see Fig. 10).~~

11 Acknowledgements

12 The study was supported by the Academy of Finland through the AMICO and A4 projects
 13 (contracts 263918 and 254195, respectively) and by the Nordic Centre of Excellence project
 14 SVALI, “Stability and Variations of Arctic Land Ice”, funded by the Nordic Top-level
 15 Research Initiative (TRI). This publication is SVALI contribution number 65. We thank the
 16 FINNARP logistics team and Antti Aarva for valuable support.

18 References

- 19 Anttila, K., Manninen, T., Karjalainen, T., Lahtinen, P., Riihelä, A., and Siljamo, N.: The
 20 temporal and spatial variability in submeter scale surface roughness of seasonal snow in
 21 Sodankylä Finnish Lapland in 2009–2010, *J. Geophys. Res. Atmos.*, 119, 9236–9252,
 22 doi:10.1002/2014JD021597, 2014.
- 23 Aoki, T., Aoki, T., Fukabori, M., Hachikubo, A., Tachibana, Y., and Nishio, F.: Effects of
 24 snow physical parameters on spectral albedo and bi-directional reflectance of snow surface, *J.*
 25 *Geophys. Res.*, 105, 10 219–10 236, 2000.
- 26 Aoki, T., Aoki, T., Fukabori, M., Tachibana, Y., Zaizen, Y., Nishio, F., and Oishi, T.:
 27 Spectral albedo observation on the snow field at Barrow, Alaska, *Polar Meteorol. Glaciol.*, 12,
 28 1–9, 1998.

- 1 Aoki, T., Hachikubo, A., and Hori, M.: Effects of snow physical parameters on shortwave
2 broadband albedos, *J. Geophys. Res.*, 108(D19), 4616, doi:10.1029/2003JD003506, 2003.
- 3 Aoki, T., Hori, M., Motoyoshi, H., Tanikawa, T., Hachikubo, A., Sugiura, K., Yasunari, T. J.,
4 Storvold, R., Eide, H. A., Stamnes, K., Li, W., Nieke, J., Nakajima, Y., Takahashi, F.:
5 ADEOS-II/GLI snow/ice products: Part II—Validation results using GLI and MODIS data,
6 *Remote Sens. Environ.*, 111, 274–290, doi:10.1016/j.rse.2007.02.035, 2007.
- 7 [Aoki, T., Kuchiki, K., Niwano, M., Kodama, Y., Hosaka, M., and Tanaka, T.: Physically
8 based snow albedo model for calculating broadband albedos and the solar heating profile in
9 snowpack for general circulation models, *J. Geophys. Res.*, 116, D11114,
10 doi:10.1029/2010JD015507, 2011.](#)
- 11 Arnaud, L., Picard, G., Champollion, N., Domine, F., Gallet, J.-C., Lefebvre, E., Fily, M., and
12 Barnola, J.-M.: Measurement of vertical profiles of snow specific surface area with a 1 cm
13 resolution using infrared reflectance: instrument description and validation, *J. Glaciol.*, 57,
14 17–29, doi:10.3189/002214311795306664, 2011.
- 15 Berisford, D. F., Molotch, N. P., Durand, M. T., Painter, T H.: Portable spectral profiler probe
16 for rapid snow grain size stratigraphy, *Cold. Reg. Sci. Technol.*, 85, 183-190, 2013.
- 17 Bohren, C. F. and Huffman, D. R.: Absorption and scattering of light by small particles.
18 Wiley, New York, 530 pp., 1983.
- 19 [Boucher, O.: On aerosol direct shortwave forcing and the Henyey–Greenstein phase
20 function. *J. Atmos. Sci.*, 55, 128–134, 1998.](#)
- 21 Carmagnola, C. M., Dominé, F., Dumont, M., Wright, P., Strellis, B., Bergin, M., Dibb, J.,
22 Picard, G., Libois, Q., Arnaud, L., and Morin, S.: Snow spectral albedo at Summit,
23 Greenland: measurements and numerical simulations based on physical and chemical
24 properties of the snowpack, *The Cryosphere*, 7, 1139-1160, doi:10.5194/tc-7-1139-2013,
25 2013.
- 26 Cauchy, A.: Note sur divers theoremes relatifs a la rectification des courbes et a la quadrature
27 des surfaces, *C.R. Acad. Sci., Paris*, vol. 13, pp.1060-1065, 1841.
- 28 Chýlek, P., Damiano, P., and Shettle, E.P.: Infrared emittance of water clouds, *J. Atmos. Sci.*,
29 49, 1459-1472, 1992.

1 Colbeck, S. C., Akitaya, E., Armstrong, R., et al.: The International Classification for
2 Seasonal Snow on the Ground, International Commission of Snow and Ice and World Data
3 Center A for Glaciology, Boulder, CO, USA, 1990.

4 Domine, F., Salvatori, R., Legagneux, L., Salzano, R., Fily, M., and Casacchia, R.:
5 Correlation between the specific surface area and the short wave infrared (SWIR) reflectance
6 of snow, *Cold Reg. Sci. Technol.*, 46(1), 60–68, doi:10.1016/j.coldregions.2006.06.002, 2006.

7 [Edwards, J.M. and Slingo, A.: Studies with a flexible new radiation code. I: Choosing a](#)
8 [configuration for a large-scale model, *Quart. J. Roy. Meteor. Soc.*, 122, 689-719, 1996.](#)

9 Fassnacht, S. R., Williams, M. W., and Corrao, M. V.: Changes in the surface roughness of
10 snow from millimetre to metre scales, *Ecol. Complexity*, 6, 221–229, 2009.

11 Fierz, C., Armstrong, R.L., Durand, Y., Etchevers, P., Greene, E., McClung, D.M.,
12 Nishimura, K., Satyawali, P.K. and Sokratov, S.A: The International Classification for
13 Seasonal Snow on the Ground. IHP-VII Technical Documents in Hydrology N°83, IACS
14 Contribution N°1, UNESCO-IHP, Paris, 2009.

15 Fily, M., Bourdelles, B., Dedieu, J. P., and Sergent, C.: Comparison of In situ and Landsat
16 Thematic Mapper derived snow grain characteristics in the Alps, *Remote Sen. Environ.*, 59,
17 452-460, 1997.

18 Flanner, M. G., and Zender, C. S.: Linking snowpack microphysics and albedo evolution, *J.*
19 *Geophys. Res.* 111, D12208, doi:10.1029/2005JD006834, 2006. Gallet, J.-C., Domine, F.,
20 Arnaud, L., Picard, G., and Savarino, J.: Vertical profile of the specific surface area and
21 density of the snow at Dome C and on a transect to Dumont D’Urville, Antarctica – albedo
22 calculations and comparison to remote sensing products, *The Cryosphere*, 5, 631–649,
23 doi:10.5194/tc-5-631-2011, 2011.

24 [Fujiyoshi, Y., and Wakahama, G.: On the snow particles comprising an aggregate, *J. Atmos.*](#)
25 [*Sci.*, 42, 1667-1674, 1985.](#)

26 Gallet, J.-C., Domine, F., Savarino, J., Dumont, M., and Brun, E.: The growth of sublimation
27 crystals and surface hoar on the Antarctic plateau, *The Cryosphere*, 8, 1205-1215,
28 doi:10.5194/tc-8-1205-2014, 2014.

- 1 Gallet, J.-C., Domine, F., Zender, C. S., and Picard, G.: Measurement of the specific surface
2 area of snow using infrared reflectance in an integrating sphere at 1310 and 1550 nm, *The*
3 *Cryosphere*, 3, 167 – 182, doi:10.5194/tc-3-167-2009, 2009.
- 4 Gay, M., Fily, M., Genthon, C., Frezzotti, M., Oerter, H., and Winther, J.-G.: Snow grain-size
5 measurements in Antarctica, *J. Glaciol.*, 48, 527-535, 2002.
- 6 Grenfell T. C., and Warren S. G.: Representation of a nonspherical ice particle by a collection
7 of independent spheres for scattering and absorption of radiation. *J. Geophys. Res.*, 104,
8 31697-31708, 1999.
- 9 Grenfell, T. C., Perovich, D. K., and Ogren, J. A.: Spectral albedos of an alpine snowpack,
10 *Cold Regions Sci. Technol.*, 4, 121-127, 1981.
- 11 Grenfell, T. C., Neshyba, S. P., and Warren, S. G.: Representation of a nonspherical ice
12 particle by a collection of independent spheres for scattering and absorption of radiation: 3.
13 Hollow columns and plates, *J. Geophys. Res.*, 110, D17203, doi:10.1029/2005JD005811,
14 2005.
- 15 Grenfell, T. C., Warren, S., and Mullen, P. C.: Reflection of solar radiation by the Antarctic
16 snow surface at ultraviolet, visible, and near infrared wavelengths, *J. Geophys. Res.*, 99,
17 18669–18684, 1994.
- 18 Hansen, J. E., and Travis, L. D.: Light scattering in planetary atmospheres, *Space Sci. Rev.*,
19 16, 527-610, 1974.
- 20 Henyey, L. G., and Greenstein, J. L.: Diffuse radiation in the galaxy, *Astrophys. J.*, 93, 70-83,
21 1941.
- 22 Hildebrand, T., and Rügsegger, P.: A new method for the model-independent assessment of
23 thickness in three-dimensional images, *J. Microsc.*, 185(1), 67-75, 1997.
- 24 Hudson, S. R., and Warren, S. G.: An explanation for the effect of clouds over snow on the
25 top-of-atmosphere bidirectional reflectance, *J. Geophys. Res.*, 112, D19202,
26 doi:10.1029/2007JD008541, 2007.
- 27 Hudson, S. R., Warren, S. G., Brandt, R. E., Grenfell, T. C., and Six, D.: Spectral
28 bidirectional reflectance of Antarctic snow: Measurements and parameterization, *J. Geophys.*
29 *Res.*, 111, D18106, doi:10.1029/2006JD007290, 2006.

- 1 Jin, Z., Charlock, T. P., Yang, P., Xie, Y., and Miller, W.: Snow optical properties for
2 different particle shapes with application to snow grain size retrieval and MODIS/CERES
3 radiance comparison over Antarctica, *Remote Sens. Environ.*, 112, 3563-3581, 2008.
- 4 Kokhanovsky, A., Rozanov, V. V., Aoki, T., Odermatt, D., Brockmann, C., Krüger, O.,
5 Bouvet, M., Drusch, M., and Hori, M.: Sizing snow grains using backscattered solar light, *Int.*
6 *J. Remote Sens.*, 32, 6975–7008, doi:10.1080/01431161.2011.560621, 2011.
- 7 Kokhanovsky, A. A., and Zege, E. P.: Scattering optics of snow, *Appl. Opt.*, 43, 1589–1602,
8 2004.
- 9 Kuchiki, K., Aoki, T., Tanikawa, T., and Kodama, Y.: Retrieval of snow physical parameters
10 using a ground-based spectral radiometer, *Appl. Opt.*, 48 (29), 5567-5582, 2009.
- 11 Kuester, M., K. Thome, K. Krause, K. Canham, and E. Whittington: Comparison of surface
12 reflectance measurements from three ASD FieldSpec FR spectroradiometers and one ASD
13 FieldSpec VNIR spectroradiometer. In: *Geoscience and Remote Sensing Symposium*, 2001.
14 *IGARSS '01, IEEE 2001 International*, Sydney, 1, 72 – 74, 2001.
- 15 Kuhn, M.: Anisotropic reflection from sastrugi fields, *Antarct. J. U. S.*, 9, 123-125, 1974.
- 16 Leroux, C., and Fily M.: Modelling the effect of sastrugi on snow reflectance, *J Geophys*
17 *Res.*, 103(E11), 25779–88, 1998.
- 18 Libois, Q., Picard, G., France, J. L., Arnaud, L., Dumont, M., Carmagnola, C., and King, M.
19 D.: Influence of grain shape on light penetration in snow, *The Cryosphere*, 7, 1803-1818,
20 2013.
- 21 Lindqvist, H., Muinonen, K., Nousiainen, T., Um, J., McFarquhar, G. M., Haapanala, P.,
22 Makkonen, R., and Hakkarainen, H.: Ice-cloud particle habit classification using principal
23 components, *J. Geophys. Res.*, 117, D16206, doi:10.1029/2012JD017573, 2012.
- 24 Liou, K. N., Gu, Y., Yue, Q., and McFarguhar, G.: On the correlation between ice water
25 content and ice crystal size and its application to radiative transfer and general circulation
26 models, *Geophys. Res. Lett.*, 35, L13805, doi:10.1029/2008GL033918, 2008.
- 27 [Liou, K. N., Takano, Y., and Yang, P.: Light absorption and scattering by aggregates:
28 Application to black carbon and snow grain, *J.Quant. Spectrosc. Radiat. Transfer*, 112, 1581–
29 1594, doi:10.1016/j.jqsrt.2011.03.007, 2011.](#)

1 Lubin, D., and Vogelmann, A. M.: The influence of mixed-phase clouds on surface shortwave
2 irradiance during the Arctic spring, *J. Geophys. Res.*, 116, D00T05,
3 doi:10.1029/2011JD015761, 2011.

4 Lyapustin, A., Gatebe, C. K., Kahn, R., Brandt, R., Redemann, J., Russell, P., King, M. D.,
5 Pedersen, C. A., Gerland, S., Poudyal, R., Marshak, A., Wang, Y., Schaaf, C., Hall, D., and
6 Kokhanovsky, A.: Analysis of snow bidirectional reflectance from ARCTAS spring-2008
7 campaign, *Atmos. Chem. Phys.*, 10, 4359-4375, doi:10.5194/acp-10-4359-2010, 2010.

8 Lyapustin, A., Tedesco, M., Wang, Y., Aoki, T., Hori, M., and Kokhanovsky, A.: Retrieval of
9 snow grain size over Greenland from MODIS, *Remote Sens. Environ.*, 113, 1976-1987, 2009.

10 Mac Arthur, A., MacLellan, C. J., and Malthus, T.: The Fields of View and Directional
11 Response Functions of Two Field Spectroradiometers, *Geoscience and Remote Sensing, IEEE*
12 *Transactions on* 50(10): 3892-3907, 2011.

13 Manninen, T.: Surface roughness of Baltic Sea ice, *J. Geophys. Res.*, 102 (C1), 1119-1139,
14 1997.

15 Mishchenko, M. M., Dlugach, J. M., Yanovitskij, E. G., and Zakharova, N. T.: Bidirectional
16 reflectance of flat, optically thick particulate layers: an efficient radiative transfer solution and
17 applications to snow and soil surfaces, *J. Quant. Spectrosc. Rad. Trans.*, 63, 409–432, 1999.

18 Mätzler, C.: Autocorrelation functions of granular media with free arrangement of spheres,
19 spherical shells or ellipsoids, *J. Appl. Phys.*, 81(3), 1509-1517, 1997.

20 Nakamura, T., Abe, O., Hasegawa, T., Tamura, R., and Ohta, T.: Spectral reflectance of snow
21 with a known grain-size distribution in successive metamorphism, *Cold Reg. Sci. Technol.*,
22 32, 13-26, 2001.

23 Neshyba, S. P., Grenfell, T. C., and Warren, S. G.: Representation of a nonspherical ice
24 particle by a collection of independent spheres for scattering and absorption of radiation: 2.
25 Hexagonal columns and plates, *J. Geophys. Res.*, 108(D15), 4448,
26 doi:10.1029/2002JD003302, 2003.

27 Nolin, A.W., and Dozier, J.: A hyperspectral method for remotely sensing the grain size of
28 snow. *Remote Sens. Environ.*, 74(2), 207–216. doi:10.1016/S0034- 4257(00)00111-5, 2000.

- 1 Painter, T. H., and Dozier, J.: Measurements of the hemispherical-directional reflectance of
2 snow at fine spectral and angular resolution, *J. Geophys. Res.*, 109, D18115,
3 doi:10.1029/2003JD004458, 2004.
- 4 Painter, T.H., Dozier, J., Roberts, D.A., Davis, R.E., and Green, R.O.: Retrieval of subpixel
5 snow-covered area and grain size from imaging spectrometer data, *Remote Sens. Environ.*, 85
6 (1), 64–77, 2003.
- 7 Painter, T. H., Molotch, N. P., Cassidy, M., Flanner, M., and Steffen, K.: Contact
8 Spectroscopy for Determination of Stratigraphy of Optical Grain Size, *J. Glaciol.*, 53, 121–
9 127, 2007.
- 10 Picard, G., Arnaud, L., Domine, F., and Fily, M.: Determining snow specific surface area
11 from near-infrared reflectance measurements: numerical study of the influence of grain shape,
12 *Cold Reg. Sci. Technol.*, 56, 10-17, 2009.
- 13 Pirazzini, R.: Surface albedo measurements over Antarctic sites in summer. *J. Geophys. Res.*,
14 109, D20118, 2004.
- 15 ~~Pirazzini, R., and Räisänen, P.: Snow particle metrics over a melting Antarctic ice sheet, in~~
16 ~~preparation.~~
- 17 Pringle, D. J., Miner, J. E., Eicken, H., and Golden, K. M.: Pore space percolation in sea ice
18 single crystals, *J. Geophys. Res.*, 114, C12017, doi:10.1029/2008JC005145, 2009.
- 19 Rizk, A., Paul, G., Incardona, P., Bugarski, M., Niemann, A., Ziegler, U., Berger, P., and
20 Sbalzarini I. F.: Segmentation and quantification of subcellular structures in fluorescence
21 microscopy images using Squash, *Nature Protocols*, 9, 586-596, 2014.
- 22 Räisänen, P., Kokhanovsky, A., Guyot, G., Jourdan, O., and Nousiainen, T.: Parameterization
23 of single-scattering properties of snow, *The Cryosphere Discuss.*, 9, 873-926,
24 doi:10.5194/tcd-9-873-2015, 2015.
- 25 Schneebeli, M., and Sokratov, S. A.: Tomography of temperature gradient metamorphism of
26 snow and associated changes in heat conductivity, *Hydrol. Process.*, 18, 3655-3665, DOI:
27 10.1002/hyp.5800, 2004.
- 28 Sjöblom A, and Smedman, A.: The turbulent kinetic energy budget in the marine atmospheric
29 boundary layer. *J Geophys Res* 107(C10):3142. doi:10.1029/2001JC001016, 2002.

- 1 Stamnes, K., Li, W., Eide, H., Aoki, T., Hori, M., and Storvold, R.: ADEOS-II/GLI snow/ice
2 products—Part I: Scientific Basis, *Remote Sens. Environ.*, 111, 258–273, 2007.
- 3 Stamnes, K., Tsay, S. C., Wiscombe, W., and Jayaweera, K: Numerically stable algorithm for
4 discrete-ordinate-method radiative transfer in multiple scattering and emitting layered media,
5 *Appl. Opt.*, 27, 2502–2509, 1988.
- 6 Tedesco, M., and Kokhanovsky, A. A.: The semi-analytical snow retrieval algorithm and its
7 application to MODIS data, *Remote Sens. Environ.*, 111, 228-241, 2007.
- 8 Vihma, T., Mattila, O.-P., Pirazzini, R., and Johansson, M. M.: Spatial and temporal
9 variability in summer snow pack in Dronning Maud Land, Antarctica, *The Cryosphere.*, 5,
10 187–201, doi:10.5194/tc-5-187-2011, 2011.
- 11 Warren, S. G.: Optical properties of snow, *Rev. Geophys.*, 20(1), 67–89, 1982.
- 12 Warren, S. G., Brandt, R. E. and O’Rawe Hinton, P.: Effect of surface roughness on
13 bidirectional reflectance of Antarctic snow, *J. Geophys. Res.*, 103, 25,789–25,807, 1998.
- 14 Warren, S. G., and Brandt, R. E.: Optical constants of ice from the ultraviolet to the
15 microwave: A revised compilation, *J. Geophys. Res.*, 113, D14220, doi:10.1029/
16 2007JD009744, 2008.
- 17 [Warren, S. G. and Clarke, A. D.: Soot in the atmosphere and snow surface of Antarctica, J.](#)
18 [Geophys. Res., 95, 1811-1816, 1990.](#)
- 19 Wiscombe, W. J.: The delta-M method: rapid yet accurate radiative flux calculations for
20 strongly asymmetric phase functions, *J. Atmos. Sci.*, 34, 1408-1422, 1977.
- 21 Wiscombe, W. J., and Warren, S. G.: A model for the spectral albedo of snow, I, Pure snow.
22 *Journal of the Atmospheric Sciences*, 37(12), 2712–2733, 1980.
- 23 Yang, P., Baum, B.A., Heymsfield, A.J., Hu, Y.X., Huang, H.-L., Tsay, S.-C., and Ackerman,
24 S.: Single-scattering properties of droxtals, *J. Quant. Spectrosc. Radiat. Transfer*, 79–80,
25 1159–1169, 2003.
- 26 Yang, P., Bi, L., Baum, B.A., Liou, K.-N., Kattawar, G.W., Mishchenko, M. I., and Cole, B.:
27 Spectrally consistent scattering, absorption, and polarization properties of atmospheric ice
28 crystals at wavelengths from 0.2 to 100 μm . *J. Atmos. Sci.*, 70, 330-347, doi:10.1175/JAS-D-
29 12-039.1, 2013.

1 Zhou, X., Li, S., and Stamnes, K.: Effects of vertical inhomogeneity on snow spectral albedo
2 and its implication for optical remote sensing of snow, *J. Geophys. Res.*, 108 (D23), 4738,
3 doi:10.1029/2003JD003859, 2003.

4 Zhuravleva, T., and Kokhanovsky, A.: Influence of surface roughness on the reflective
5 properties of snow, *J. Quant. Spectrosc. Radiat. Transfer.*, 112, 1353–1368,
6 doi:10.1016/j.jqsrt.2011.01.004, 2011.

7

1 Table 1. Snow pit and spectral reflectance measurement times during clear and overcast days, mean solar zenith angle (θ_0) during the
2 clear-sky reflectance measurements, as well as the mean value and standard deviation of the air temperature (T_a), relative humidity (RH), wind
3 speed (V), and wind direction (Dir) during the time frame covered by the snow and reflectance measurements. The last column gives the
4 mean, minimum, and maximum air temperature in the 24 hours preceding the corresponding snow pit measurements ($\overline{T24_a}$, $T24_{a,min}$, and
5 $T24_{a,max}$, respectively). Local solar time is approximately UTC – 54 minutes.

Date	Sky	Time of snow pit (UTC)	Time of Reflectance (UTC)	θ_0	T_a (°C)	RH (%)	V (m/s)	Dir (°)	$\overline{T24_a}$ [$T24_{a,min}$, $T24_{a,max}$]
23 Dec	Overc	10:19	11:50		-6.0±0.3	83 ± 5	5.7 ± 0.5	81 ± 5	-6.1[-7.7,-4.8]
26 Dec	Clear	11:35	12:25	49.9	-5.3±0.3	64 ± 7	2.1 ± 0.7	133 ± 38	-7.2[-13.4,-4.2]
29 Dec	Clear	10:55	14:19	51.1	-4.4±0.4	58 ± 5	2.6 ± 1.0	140 ± 18	-6.0[-9.1,-3.0]
5 Jan	Clear	9:50	10:19	55.1	0.5±0.6	57 ± 4	4.9 ± 1.3	65 ± 6	-0.4[-5.7,3.1]
6 Jan	Clear	10:00	10:34	54.5	-1.3±0.3	58 ± 2	4.2 ± 0.7	80 ± 12	-1.8[-7.6,1.1]
12 Jan	Clear	11:17	9:57, 11:54	54.9	-4.2±0.5	72 ± 5	2.3 ± 0.8	116 ± 52	-3.2[-7.5,-0.4]
14 Jan	Overc	11:10	9:44		-2.5±0.1	76 ± 1	5.6 ± 0.4	74 ± 7	-4.2[-6.3,-2.5]
19 Jan	Clear	10:50	9:44, 11:50	56.8	-3.9±0.3	77 ± 1	7.9 ± 1.3	166 ± 2	-2.1[-6.1,0.8]

1 Table 2. Uncertainties on the vertical profiles of snow temperature (T_{snow}) and density
 2 (ρ_{snow}), calculated as the square root of the sum of the squares of instrumental error and intra-
 3 pit variability. The intra-pit variability is given in parenthesis.

4

	Surface	2.5 cm	5 cm	10 cm	15 cm	20 cm
T_{snow} (°C)	$\pm 0.3(\pm 0.1)$	$\pm 0.3(\pm 0.1)$	$\pm 0.3(\pm 0.1)$	$\pm 0.30(\pm 0.05)$	$\pm 0.3(\pm 0.1)$	$\pm 0.3(\pm 0.1)$
ρ_{snow} (kg m ⁻³)	$\pm 45 (\pm 16)$		$\pm 13 (\pm 10)$	$\pm 15 (\pm 12)$		$\pm 14 (\pm 12)$

5

6

1 Table 3. Classification of size and shape of the observed surface snow particles
 2 according to Fierz et al. (2009). See Sect. 2.3 for explanation of the shape codes.

<u>Date</u>	<u>Greatest dimension (mm) / shape class</u>
<u>23 Dec</u>	<u>0.2-0.5 / RGsr, 0.5-1 / RGxf, 1-1.5 / Agg^(*)</u>
<u>26 Dec</u>	<u>0.1-0.6 / FCxr</u>
<u>29 Dec</u>	<u>0.2-0.8 / RGl, 1-3 / MFpc</u>
<u>5 Jan</u>	<u>0.1-0.5 / FCsf, 1-2 / MFpc, 1-2 / SHxr</u>
<u>6 Jan</u>	<u>0.1-0.5 / FCsf, 1-2 / MFpc, 1-2 / SHxr</u>
<u>12 Jan</u>	<u>1-1.3 / SHsu, 1-2 / MFpc</u>
<u>14 Jan</u>	<u>0.1-0.5 / DFdc, 1-2 / MFpc</u>
<u>19 Jan</u>	<u>0.2-0.7 / PPco, 0.2-0.7 / PPnd, 1-2 / MFpc</u>

3 (*) Agg (Aggregate) does not belong to the shape classification of Fierz et al. (2009), but it is
 4 adopted in both observational studies (Fujiyoshi and Wakahama, 1985) and snow models (Jin
 5 et al., 2008; Liou et al., 2011; Yang et al., 2013).

6

1 Table 43. Total 5% and 95% errors of α (in percentages) calculated according to
 2 equations AB1 and AB2 in Appendix AB, averaged over the examined clear and overcast
 3 days.

4

	$\lambda < 1.8 \mu\text{m}$		$\lambda > 1.8 \mu\text{m}$	
	5%	95%	5%	95%
Clear-sky days	-9	+11	-11	+13
Overcast days	-9	+9	-11	+12

5

6

1 | Table 54. Mean surface albedo ($\overline{\alpha_{b,\Delta\lambda}}$) and net shortwave radiation ($\overline{Sw_{n\Delta\lambda}}$, Wm^{-2})
2 | integrated over three distinct wavebands ($\Delta\lambda = 1.0\text{-}1.4 \mu\text{m}$, $1.4\text{-}2.5 \mu\text{m}$, and $1.0\text{-}2.5 \mu\text{m}$)
3 | during overcast and clear-sky conditions. “Obs” refers to values obtained using the
4 | reflectance-derived albedo, “Bias S” and “Bias D” are the mean biases between model- and
5 | reflectance-derived integrated quantities obtained using spheres and droxtals, respectively.

		Overcast			Clear-sky		
		Obs	Bias S	Bias D	Obs	Bias S	Bias D
$\Delta\lambda$ (μm)							
$\overline{\alpha_{b,\Delta\lambda}}$	1.0-1.4	0.62	-0.08	-0.01	0.53	0.07	0.14
	1.4-2.5	0.12	-0.07	-0.04	0.08	-0.02	0
	1.0-2.5	0.51	-0.08	-0.02	0.37	0.04	0.09
$\overline{Sw_{n\Delta\lambda}}$	1.0-1.4	19	4	1	48	-7	-15
	1.4-2.5	13	1	1	55	1	0
	1.0-2.5	32	6	1	104	-6	-15

6

7

1 | Table 65. Mean optical effective radius ($\overline{r_{oeff}}$, mm) obtained from the measurement-
 2 | derived surface albedo at four 0.1 μ m-wide wavebands centered at 1.05, 1.28, 1.70, and 2.20
 3 | μ m. The effective variance used in the model calculations is that at the surface layer. The
 4 | standard deviation of r_{oeff} among the eight case studies is given in parenthesis.

Central wavelength (μ m)	$\overline{r_{oeff}}$ for spherical shape (mm)	$\overline{r_{oeff}}$ for droxtal shape (mm)
1.05	0.26 (0.12)	0.43 (0.21)
1.28	0.20 (0.07)	0.32 (0.11)
1.70	0.11 (0.03)	0.16 (0.04)
2.20	0.13 (0.04)	0.18 (0.05)

5

6

1 Table A1. List of Acronyms and Symbols

ASD = FieldSpec JR spectroradiometer, manufactured by Analytical Spectral Devices Inc., now PANalytical
BRDF = bidirectional reflectance distribution function
DISORT = Discrete Ordinates Radiative Transfer Program for a Multi-Layered Plane-Parallel Medium
$E05_{r_{eff},v_{eff}}$ = 5% error of the effective radius/variance, i.e. the difference between the lower limit of the 90% confidence interval and the best estimate
$E05_{r_{pr}}$ = 5% representativeness error of the SSK metric
$E05_{sub}$ = 5% subjectivity error of the SSK metric
$E05_{\Delta\alpha}$ = 5% error of the bias between model- and measurement-derived albedo
$E05_{\Phi}^2$ = 5% error of the parameterized Φ
$E05_{\alpha,mod}$ = 5% error of the modeled albedo applying the SSK metric
$E05_{\alpha,obs}$ = 5% error of the albedo derived from nadir reflectance measurements
$E95_{r_{eff},v_{eff}}$ = 95% error of the effective radius/variance, i.e. the difference between the upper limit of the 90% confidence interval and the best estimate
$E95_{r_{pr}}$ = 95% representativeness error of the SSK metric
$E95_{sub}$ = 95% subjectivity error of the SSK metric
$E95_{\Delta\alpha}$ = 95% error of the bias between model- and measurement-derived albedo
$E95_{\Phi}^2$ = 95% error of the parameterized Φ
$E95_{\alpha,mod}$ = 95% error of the modeled albedo applying the SSK metric
$E95_{\alpha,obs}$ = 95% error of the albedo derived from nadir reflectance measurements
FOV = field of view
F_0 = incident irradiance at the solar zenith angle θ_0 ($\text{W m}^{-2} \mu\text{m}^{-1}$)
I_n = radiance reflected into the nadir direction

I_r = radiance reflected into a particular direction ($\text{W m}^{-2} \text{sr}^{-1} \mu\text{m}^{-1}$)

L_i = dimension of the i^{th} particle

NIR = near-infrared light (0.7-1.0 μm)

Q_{ext} = extinction efficiency

SR = severely roughened

SSA = specific surface area of the snow particle population

SSPs = single-scattering properties

SWIR = shortwave infrared light (1.0-2.5 μm)

SWIR1 = shortwave infrared light (1.0-1.83 μm): spectral region of the second ASD sensor

SWIR2 = shortwave infrared light (1.83-2.5 μm): spectral region of the third ASD sensor

S_{wn} = broadband net shortwave radiation (0.35-2.5 μm) absorbed by the snow surface

$\overline{S_{\text{wn}}}_{\Delta\lambda}$ = mean net shortwave radiation integrated over a distinct waveband

T_{snow} = snow temperature

VIS = visible light (0.4-0.7 μm)

VNIR = visible and near-infrared (0.35-1.0 μm): spectral region of the first ASD sensor

bw = black and white

g = asymmetry parameter

m_2, m_3, m_4 = second, third, and fourth moment of the measured metric distribution

r_i = geometrical radius of the scattering particle

r_{eff} = effective radius of the measured metric distribution

r_{oeff} = optically equivalent effective radius

r_{λ} = mean optically equivalent effective radius in the 0.1 μm -wide waveband centered on the wavelength λ

v_{eff} = effective variance of the measured metric distribution

r_{VA} = volume-to-surface area equivalent radius of the measured metric distribution

r_{VP} = volume-to-projected area equivalent radius of the measured metric distribution

$\Delta_{tilt,down}$ = positive bias in reflectance/albedo due to the tilting of the snow surface in the downhill direction

$\Delta_{tilt,up}$ = negative bias in reflectance/albedo due to the tilting of the snow surface in the uphill direction

Δz = geometrical thickness of a snow layer

Φ = anisotropic reflectance factor

Φ_n = anisotropic reflectance factor in the nadir direction

α = hemispherical spectral albedo

α_b = broadband albedo

$\overline{\alpha_{b,\Delta\lambda}}$ = mean surface albedo integrated over a distinct waveband

θ_0 = solar zenith angle

$\theta_{0,eff}$ = effective solar zenith angle

θ_v = viewing zenith angle

λ = wavelength

ρ_{snow} = snow density

ρ_{ice} = ice density

σ_{ref} = error in horizontal leveling of the reference spectralon

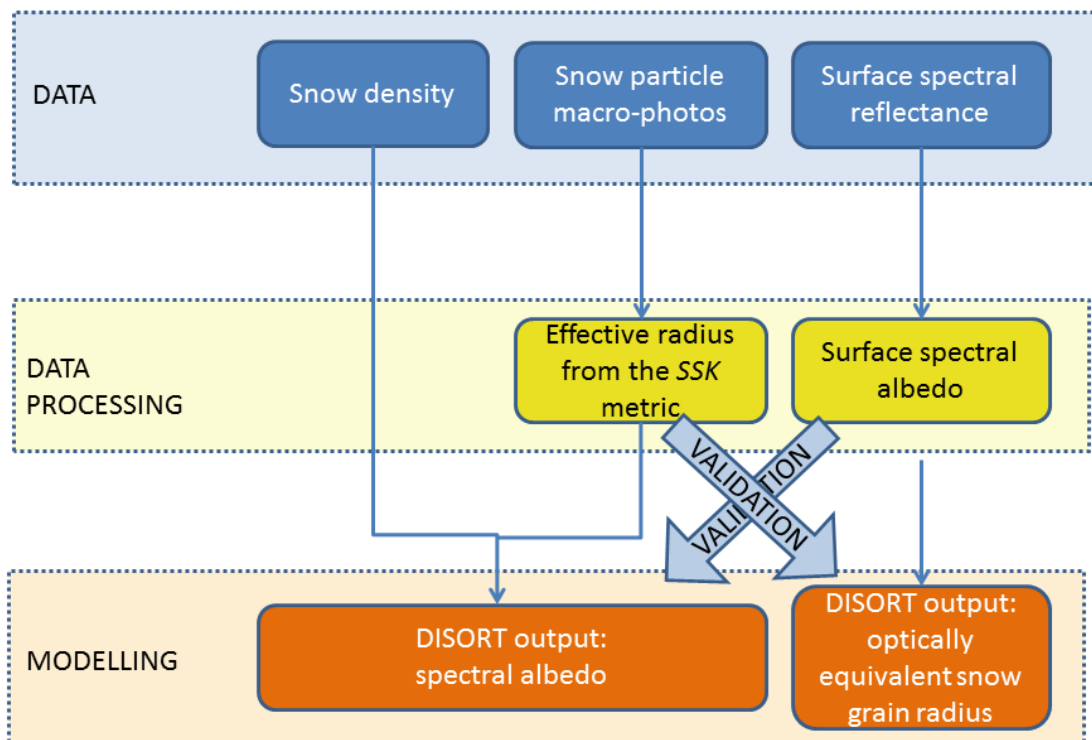
σ_{rpt} = error in repeatability of the snow reflectance

τ = optical thickness of a snow layer

ϕ = relative azimuth angle

ω = single-scattering albedo

2D = two-dimensional



1

2 Figure 1. Work flow diagram.

3

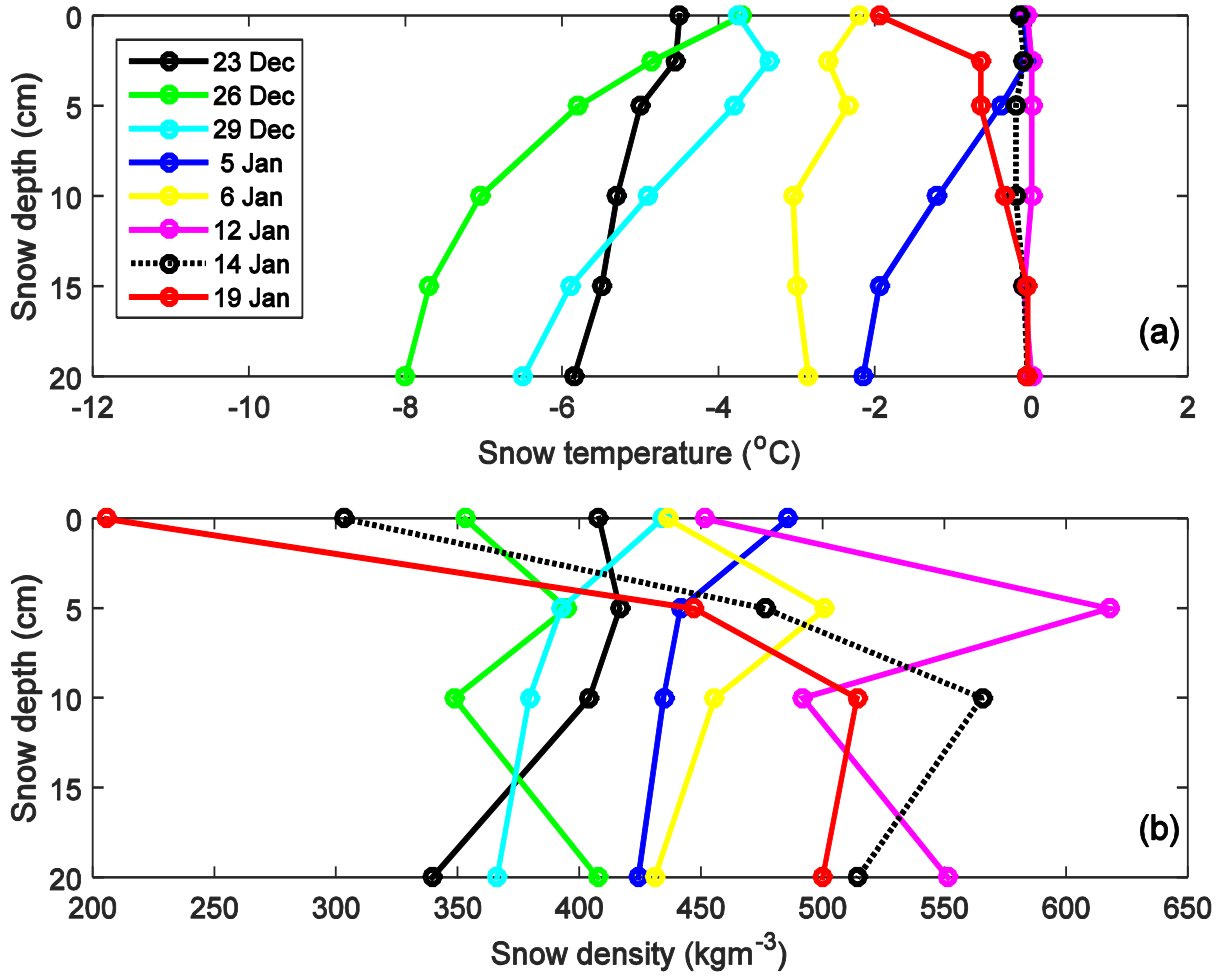
4

5

6

7

1



2

3 Figure 2. Vertical profiles of snow temperature and density in the uppermost 20 cm of
4 the snowpack for the analyzed clear and overcast cases. Each profile results from the average
5 of two almost simultaneous profiles, taken 0.4 m apart. The surface density measurements
6 were taken with a 2-cm-tall sampler, and therefore represent an average of the uppermost 2
7 cm of the snowpack. At the deeper layers, the snow density samples were taken using
8 cylinders with axis centered at 5, 10, 15 and 20 cm depths.

9

10

11



1
2

3 Figure 3. ASD spectroradiometer measuring snow reflectance as the surface texture changed
4 over the measuring period: a very smooth surface on 29 December 2009 (a), a rough surface
5 on 5 January 2010 (b), and a moderately rough surface on 19 January 2010, after a light
6 snowfall (c).

7
8
9



1

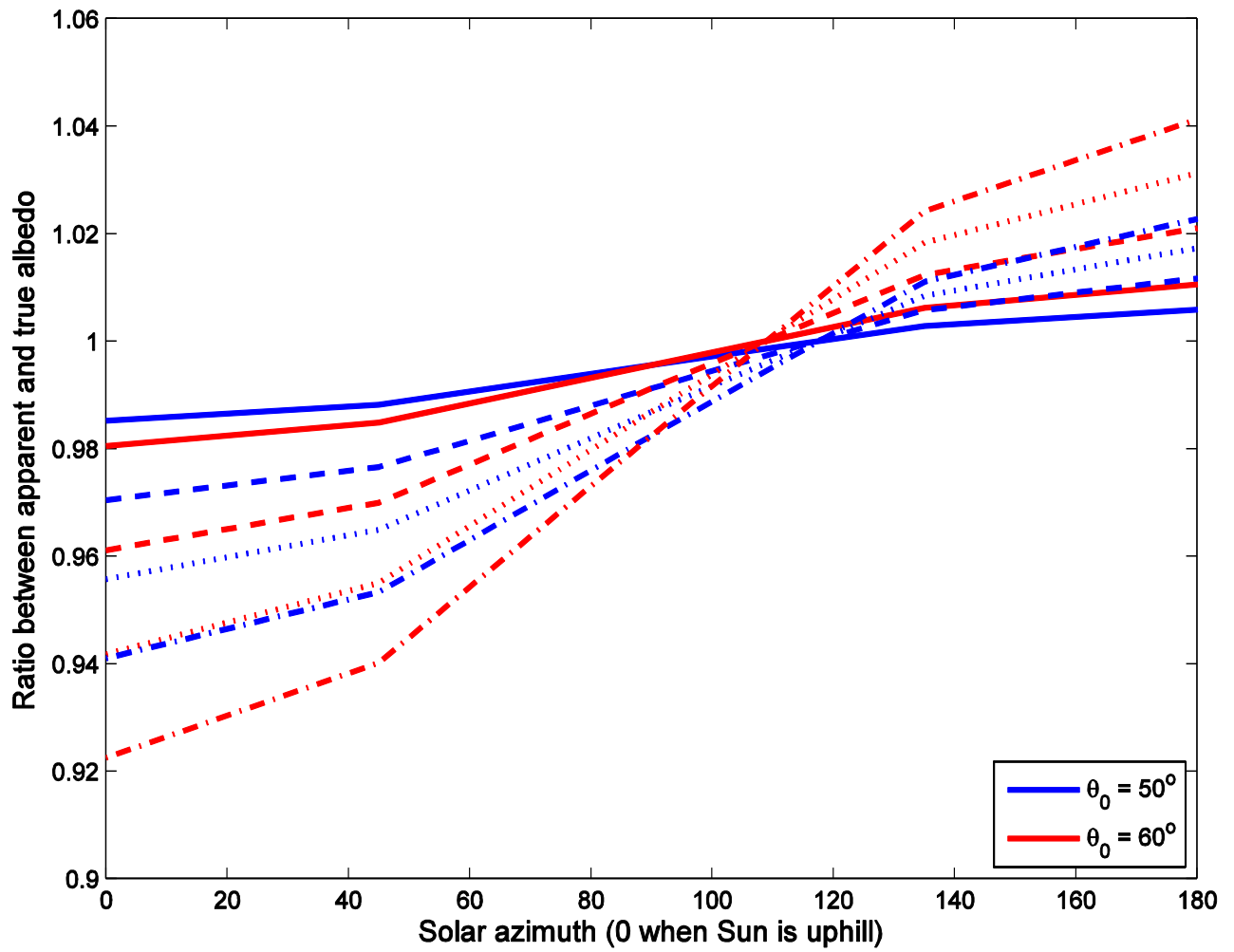
2 Figure 4. The cave dug in the snowpack (a) created a cold environment, sheltered from wind
3 and radiation, which was suitable for snow macro-photography (b). Photos by Timo Palo.

4

5

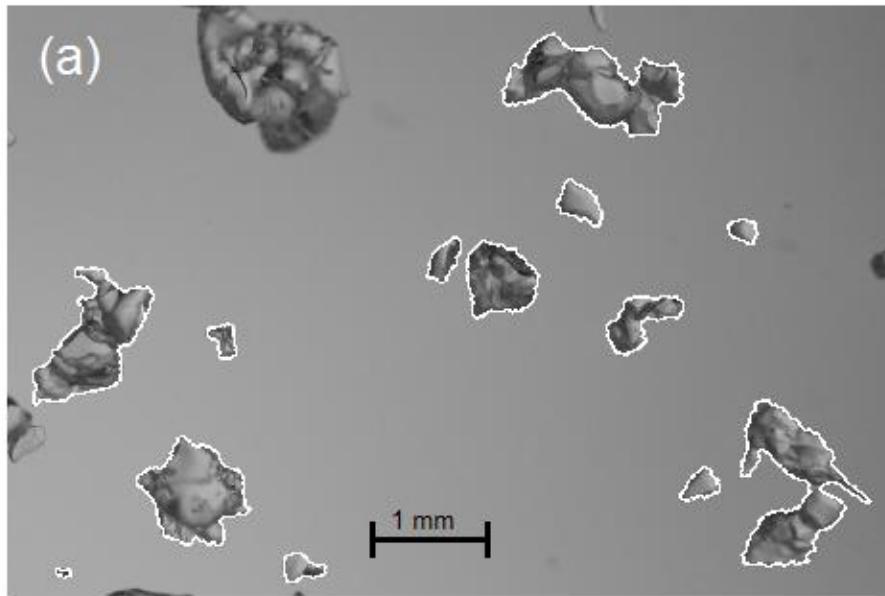
6

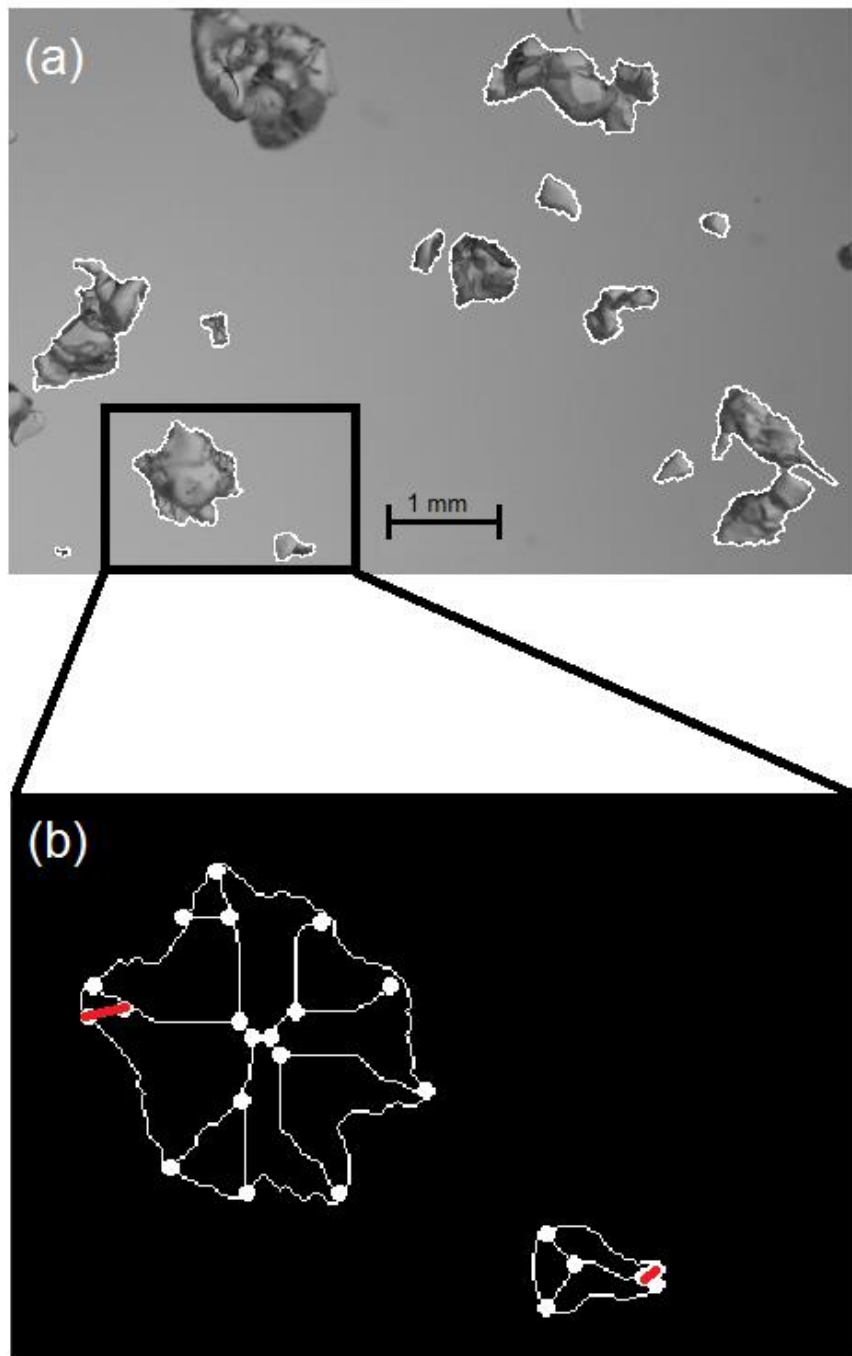
7



1
2
3
4
5
6

Figure 5. Ratio between apparent and true albedo calculated according to equation (4) in Grenfell et al. (1994) as a function of solar azimuth. Blue and red lines correspond to solar zenith angles (θ_0) of 50° and 60° , respectively. Surface slope angles of 0.5° , 1° , 1.5° , and 2° are marked with continuous, dashed, dotted, and dashed-dotted lines, respectively.

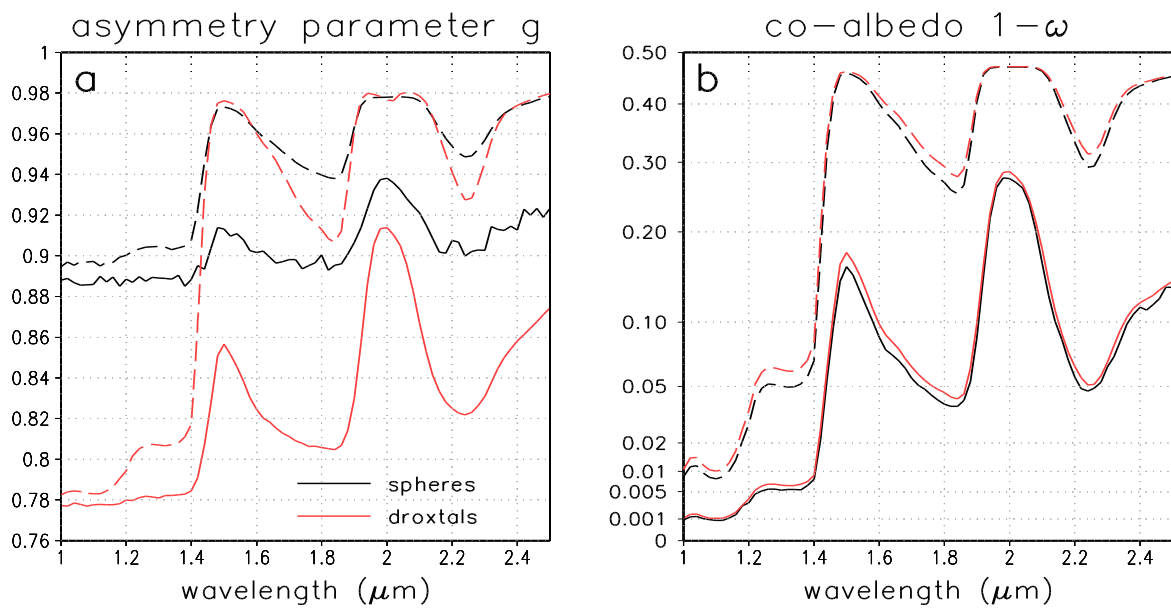




1

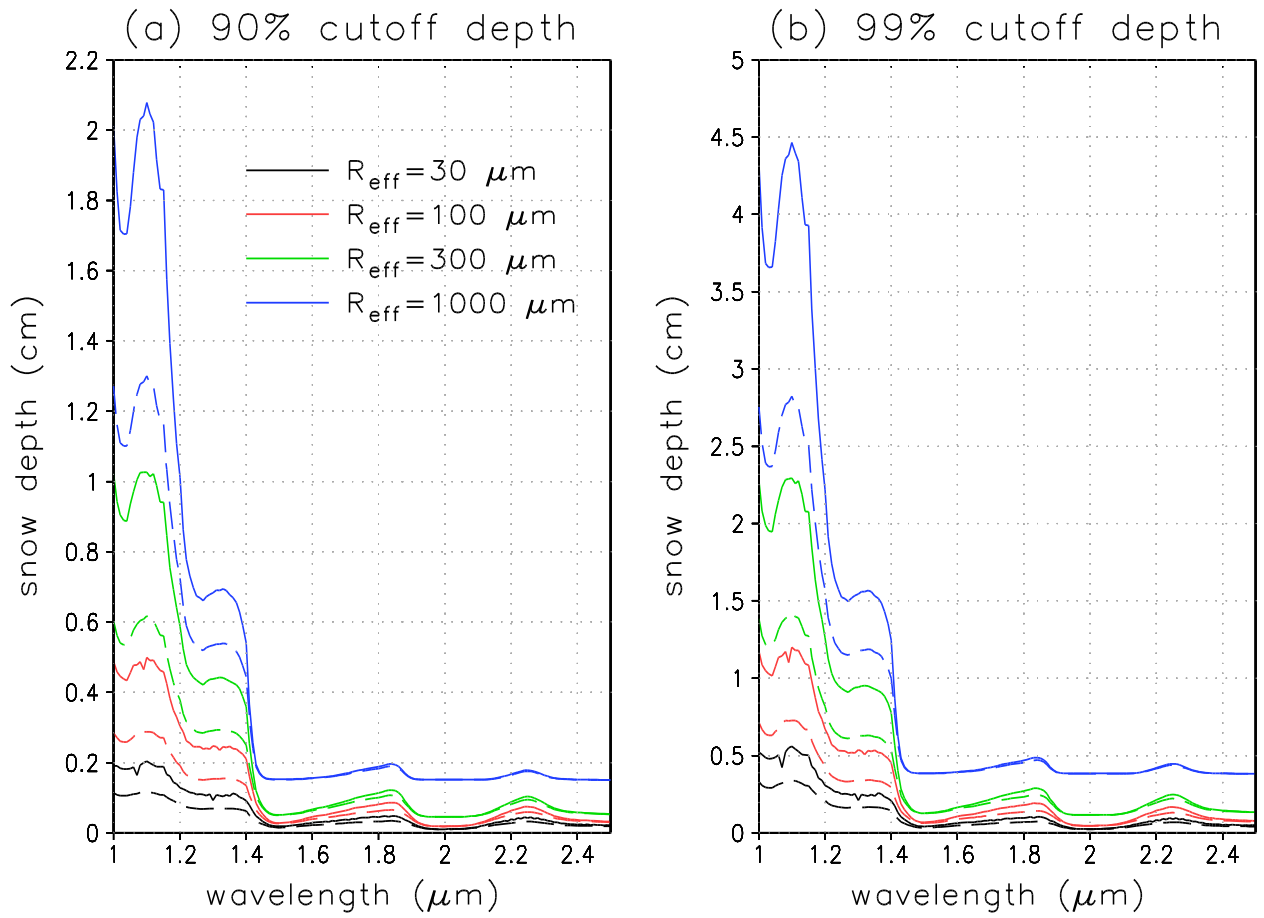
2 Figure 6. Example of a segmented image from 29 December 2009: the segmented outlines are
3 overlaid with the original image (a), and two detected particles are magnified (b) to illustrate
4 with the skeleton (inner white lines), the skeleton endpoints (white dots at the particle
5 border), and branch points (white dots along the junction nodes of the skeletons). The shortest
6 of the skeleton branches, defined here as the Euclidean distances between endpoints and
7 nearest branch point, (SSK metric) are marked in red and correspond to the SSK metric.

8



1
 2 Figure 7. (a) Asymmetry parameter g and (b) single-scattering co-albedo $1-\omega$ for spheres
 3 (black lines) and severely roughened droxtals (red lines), for two values of volume-to-
 4 projected area equivalent radius: $r_{VP} = 50 \mu\text{m}$ (solid lines) and $r_{VP} = 500 \mu\text{m}$ (dashed lines).
 5

1

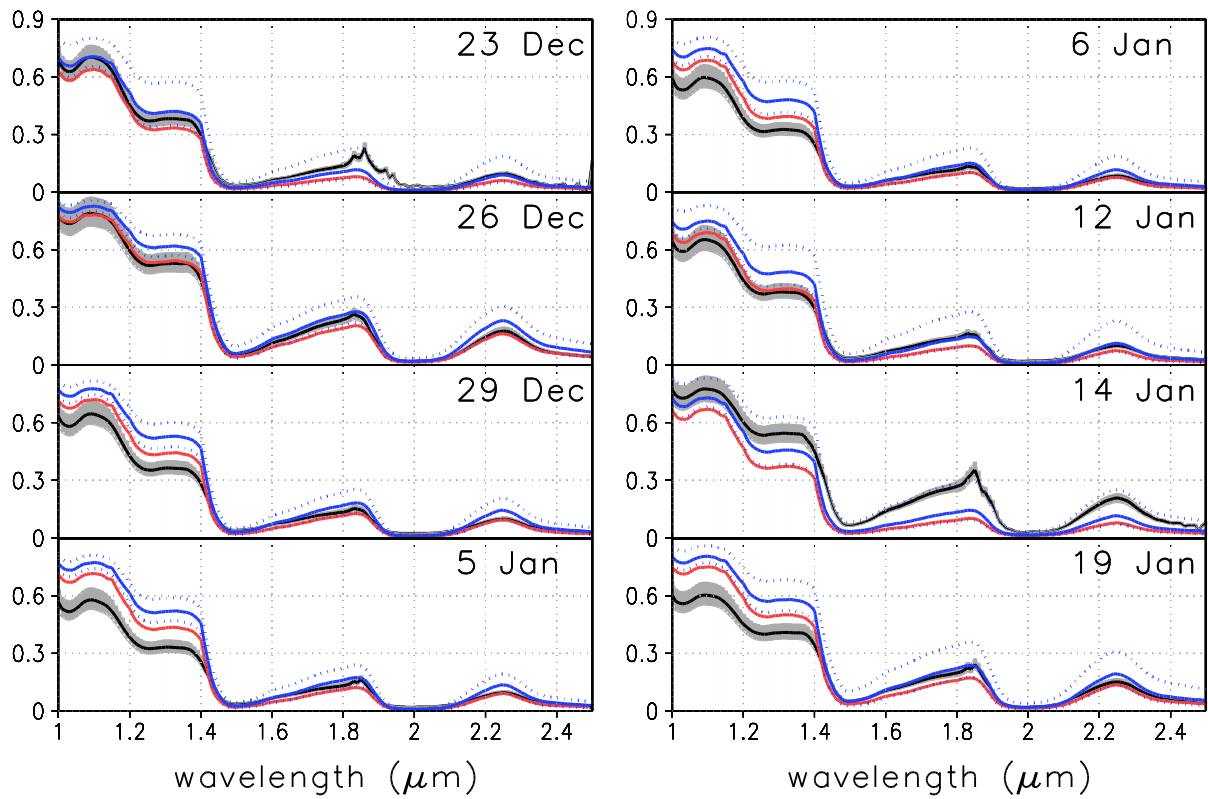


2

3

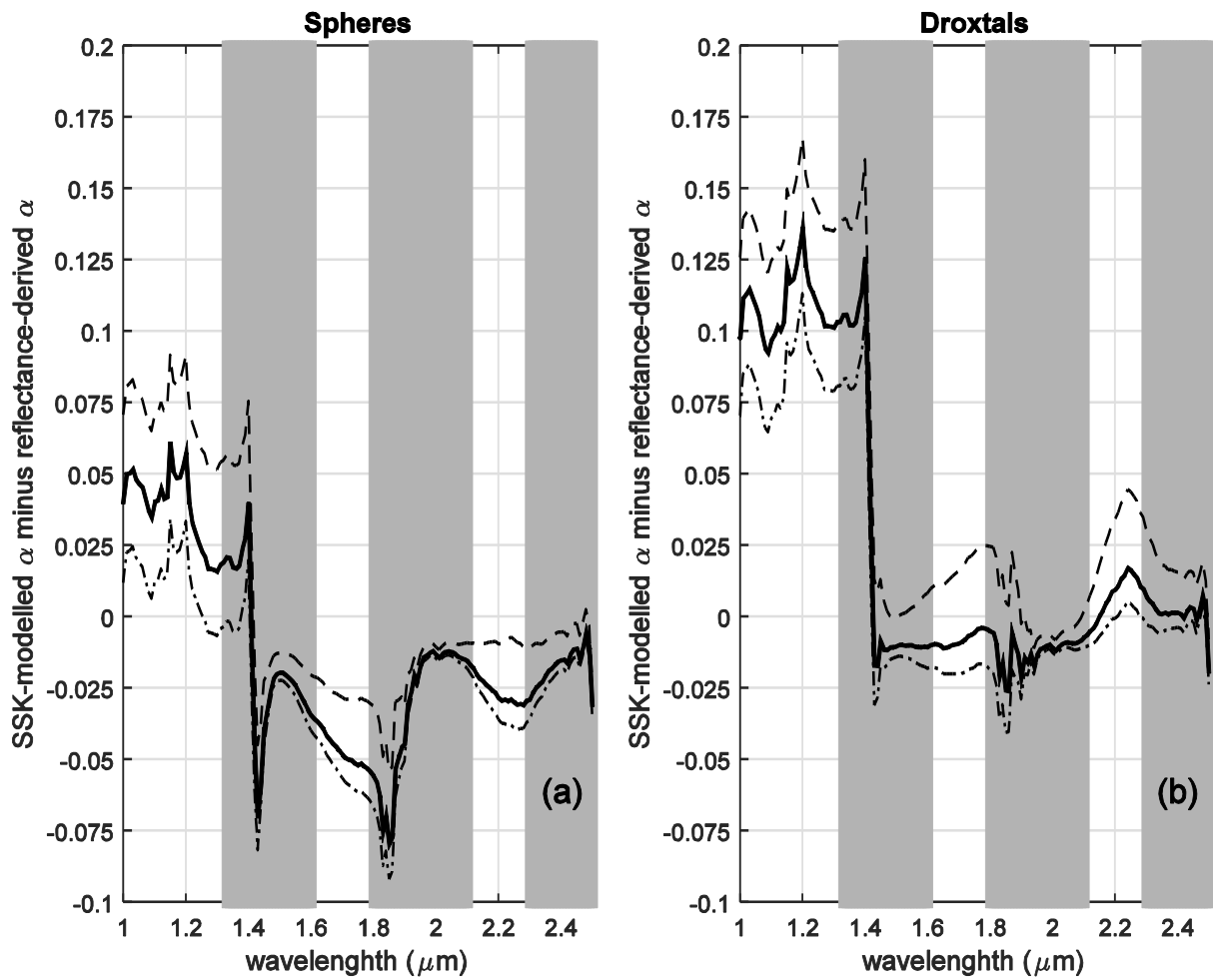
4 Figure 8. Spectral 90% (a) and 99% (b) cutoff depth of the semi-infinite albedo in the
5 SWIR region for diffuse incident radiation.. Snow density is 400 kg m^{-3} . The cases of
6 effective particle radius of 0.03, 0.1, 0.3, and 1 mm (black, red, green, and blue lines,
7 respectively) are illustrated for the assumption of spherical shapes (continuous lines) and
8 droxtal shapes (dashed lines), for a mono-disperse size distribution.

9



1
2

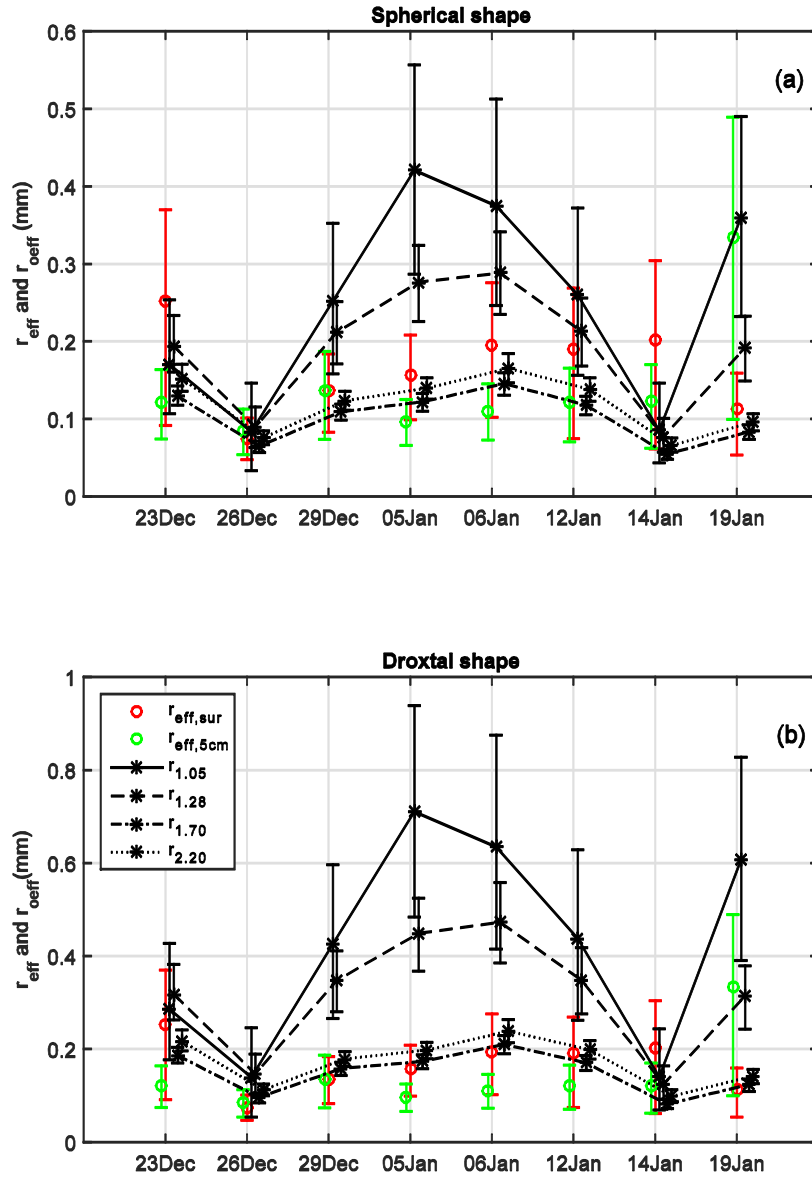
3 Figure 9. Spectral snow albedo obtained from reflectance measurements (black line) and
 4 calculated with DISORT using spherical particle shapes (red line) and droxtal particle shapes
 5 (blue line) for all case studies. In the model calculations, we applied the observed snow
 6 density and the grain distribution based on the *SSK* metric. The grey shaded areas mark the
 7 total uncertainties on the albedo derived from reflectance observations (Eqs. (A1) and
 8 (A2) in Appendix A), while the blue dotted lines represent the uncertainty in the droxtal
 9 model calculations due to the uncertainty in the metric distributions (Eqs. (A3) and (A4) in
 10 Appendix A). For the calculations with spheres, the magnitude of uncertainty is comparable
 11 to the uncertainty in the droxtal calculations (not shown).



1

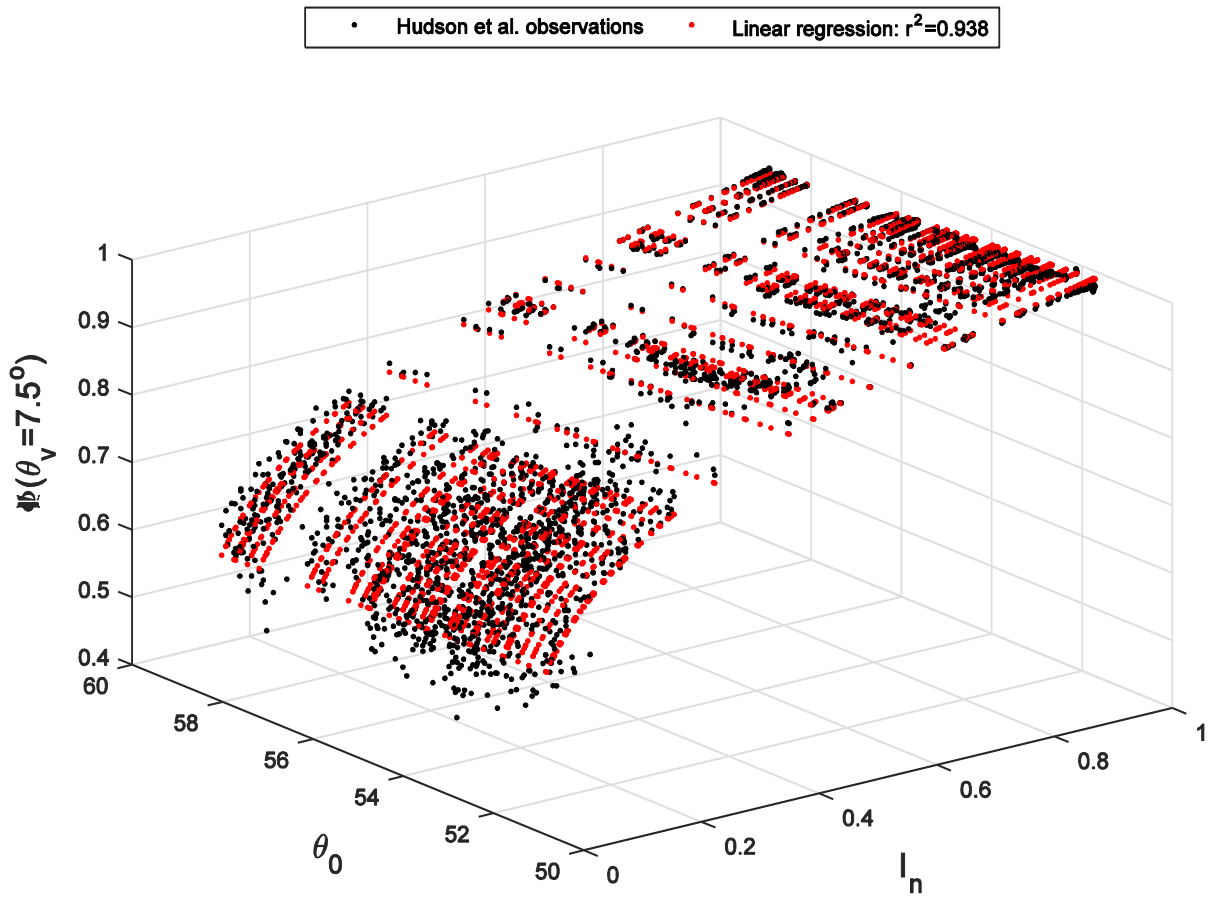
2

3 Figure 10. Mean difference between model- and reflectance-derived albedo for spherical
 4 (a) and droxtal (b) particle shape. Shaded areas correspond to wavebands where the signal-to-
 5 noise ratio of the reflectance measurements was very low. Dashed black lines mark the 5%
 6 and 95% confidence limits of the mean bias (see Appendix [AB3](#)).



1
2
3
4
5
6
7
8
9
10
11
12

Figure 11. r_{eff} obtained from the distributions of shortest skeleton branches at the surface ($r_{eff,sur}$, red circles) and at 5 cm depth ($r_{eff,5cm}$, green circles), and r_{oeff} derived with DISORT from spectral albedo observations at the wavebands centered on 1.05, 1.28, 1.70, and 2.20 μm (stars with continuous, dashed, dashed-dotted, and dotted lines, respectively) during the eight case studies, for spherical (a) and droxtal (b) particle shapes. Error bars represent the uncertainties in the data and in the model calculations: for $r_{eff,sur}$ and $r_{eff,5cm}$, the uncertainty is calculated according to Eqs. (A3) and (A4) in Appendix A, while for $r_{1.05}$, $r_{1.28}$, $r_{1.70}$, and $r_{2.20}$ the uncertainty results from the propagation of the errors in the particle metrics to the modelled albedo ($E05_{\alpha,mod}$ and $E95_{\alpha,mod}$ described in Appendix A3).



1
2
3
4
5
6
7
8
9
10

Figure BA1. Anisotropic reflectance factor (Φ) for viewing zenith angle θ_v equal to 7.5° calculated from snow reflectance measurements at Dome Concordia (Antarctic Plateau) by Hudson et al. (2006) versus solar zenith angle θ_0 and nadir reflectance I_n (black dots). The red dots correspond to the multi-linear regression of the logarithm of Φ as a function of the logarithm of spectral albedo and the cosine of θ_0 (see Eq. BA5).